Diogo Vieira Pedro Marques Saraiva

Licenciado em Engenharia de Micro e Nanotecnologias

Electro-optical devices based on cellulose nanocrystals

Dissertação para obtenção do Grau de Mestre em
Engenharia de Micro e Nanotecnologias

Orientadora: Professora Doutora Susete Fernandes, Investigadora em Pós-doutoramento, CENIMAT/I3N- Departamento de Ciência dos Materiais, Faculdade de Ciências e Tecnologia da Universidade Nova de Lisboa

Co-orientador: Professor Doutor Pedro Almeida, Professor Adjunto, Departamento de Física, Instituto Politécnico de Lisboa ISEL/IPL

Júri

Presidente: Doutor Rodrigo Ferrão Paiva Martins, Professor Catedrático, FCT-UNL

Arguente: Doutora Maria Helena Godinho, Professora Associada com Agregação, FCT-UNL

Vogal: Doutora Susete Fernandes, Investigadora em Pós-doutoramento, FCT-UNL

FACULDADE DE CIÊNCIAS E TECNOLOGIA
UNIVERSIDADE NOVA DE LISBOA

Junho, 2018

Electro-optical devices based on cellulose nanocrystals

Acknowledgements

Em primeiro lugar, quero agradecer à nossa instituição, a Faculdade de Ciências e Tecnologia da Universidade Nova de Lisboa, ao Departamento das Ciências dos Materiais e ao CENIMAT por fazerem os anos de licenciatura e mestrado passarem num ápice.

À professora Susete, a minha orientadora: não consigo enfatizar o quão grato estou por tudo o que fez este último ano. Muito obrigado por todo o tempo e paciência dispensados. Ao professor Pedro, o meu orientador, ao qual agradeço sinceramente por toda a sua disponibilidade e motivação, especialmente nesta reta final. À professora Godinho, por me ensinar muito do que acabei por escrever nesta tese, tanto nas aulas como fora delas. Agradeço também a toda a gente no laboratório 107, bem como a todos os investigadores/professores que me tenham ajudado, direta ou indiretamente, a concluir esta dissertação. De forma muito literal, esta tese não existiria se não fossem vocês.

À Cláudia e ao André. Tenho imensa sorte por ter feito a tese ao lado de pessoas tão toleráveis como vocês.

Aos manos do chat, as pessoas mais genuinamente engraçadas que conheço, não ironicamente. Ao João, Ricardo, Nuno, Manuel, Simão, Sabino, Bernardo, Rodrigo, Guilherme e Fred. Enumerei-vos porque parece um agradecimento mais significativo e sincero.

Aos manos e manas que não sejam do chat, por me terem moldado para ser o que sou hoje, de uma maneira ou de outra.

À Filipa. Ia me esquecendo de a meter aqui, mas mandou mensagem agora, por isso está aqui na versão final. “Agradeço à Filipa por me tirar a Netflix todos os meses" é o que ela sugeriu que eu dissesse.

Por último, aos meus pais, pelo apoio e paciência incondicionais ao longo destes anos. À Marta, pelos desenhos. Obrigado pelos desenhos. À avó, pela constante enxurrada de prendas e carinho. Ao tio e à tia, por fazerem parte do meu percurso de vida até hoje como “os tios fixes”.

Obrigado por tudo.

This work was funded by FEDER funds through the COMPETE 2020 Program and National Funds through FCT - Portuguese Foundation for Science and Technology under the projects numbers POCI-01-0145-FEDER-007688 (Reference UID/CTM/50025), PTDC/FIS-NAN/0117/2014 and also by M-ERA.NET, a EU funded network, for project 2/0007/2016 – CellColor.

Resumo

A auto-organização de nanocristais de celulose (NCC) em suspensão, retida da evaporação do solvente, tende a formar filmes estruturalmente coloridos, que apresentam anisotropia ótica visto que conseguem seletivamente refletir luz circularmente polarizada à esquerda e transmitir luz circularmente polarizada à direita. No entanto, devido à heterogeneidade do arranjo nemático quiral, originando diferentes valores de passo no filme, uma resposta ótica sem a transmissão total de luz no canal de luz circularmente polarizada à direita é observada. O objetivo desta dissertação é melhorar esta resposta ótica em ambos os canais de luz.

Foram obtidos filmes sólidos de NCC (com espessuras de ~100 μm) com diferentes valores de passo, que apresentam uma largura espectral de 200 nm, por sua vez atribuído a variações no passo helicoidal. De forma a reduzir estas heterogeneidades, um filme fino de NCC em forma de gota (12 μm) foi produzido usando uma taxa de evaporação controlada, resultando em melhor transmissão de luz circularmente polarizada à direita. Quando a auto-organização de uma suspensão de NCC é sujeita a um campo magnético forte (7.05 T), um filme fino homogéneo (16 μm) é produzido, com uma largura espectral mais estreita (100 nm) e uma transmissão de luz circularmente polarizada direita quase total.

Este último filme, se impregnado com um cristal líquido nemático (5CB, que converte a fase da luz polarizada de esquerda para direita, ao funcionar como uma lâmina de retardação de meia onda), mostra uma resposta ótica refletiva extensivamente homogénea em ambos os canais de luz. Este trabalho mostra que a resposta ótica de filmes finos de NCC estruturalmente coloridos pode ser melhorada pela aplicação de um campo magnético forte, abrindo assim novas possibilidades para o seu uso em dispositivos eletro-óticos.

Palavras-chave: Filmes de NCC estruturalmente coloridos, luz circularmente polarizada, campo magnético, dispositivo eletro-ótico, cristais líquidos

Abstract

The self-assembly of cellulose nanocrystals (CNC) in suspension can, upon solvent drying, form structurally colourful films presenting optical anisotropy, since they selectively reflect left circular polarised (LCP) light and transmit right circular polarised (RCP) light. However, due to the films' heterogeneous chiral nematic arrangement, which leads to different pitch sizes, an optical response without full RCP light transmission is observed. The goal of this dissertation is to improve this optical response in both light channels.

Freestanding CNC films (~100 µm in thickness) with different pitch sizes were obtained, presenting a spectral width of 200 nm, attributed to variations in the helical pitch. To reduce these heterogeneities, a thin (12 µm) drop-cast CNC film was produced using a controlled evaporation rate, with increased RCP light transmission. When the self-assembly of a CNC suspension is subjected to a strong magnetic field (7.05 T), a homogeneous thin film (16 µm) is produced, with a narrower spectral width (100 nm) and a quasi-total RCP transmission.

This latter film, if impregnated with a nematic liquid crystal (5CB, acting as a half-wave retardation plate which converts the handedness of the polarised light from left to right), shows an area-wide homogeneous optical reflection response in both light channels. This work shows that the optical response of structurally colored thin CNC films can be improved by application of a strong magnetic field, which opens new possibilities for its use in electro-optical devices.

Keywords: Structurally coloured CNC films, circularly polarised light, magnetic field, electro-optical device, liquid crystals

Table of contents

ACKNOWLEDGEMENTS V

RESUMO VII

ABSTRACT IX

LIST OF FIGURES XIII

LIST OF TABLES XVII

ACRONYMS XIX

1 INTRODUCTION 1

1.1 Liquid crystals 1

1.2 Cellulose and its derivatives 4

1.3 Electro-optical devices and interactions with liquid crystals 5

2 MATERIALS AND METHODS 9

2.1 Production of CNC freestanding films and droplets 9

2.2 Electro-optical device assembly 9

2.3 Characterisation 10

3 RESULTS AND DISCUSSION 13

3.1 CNC characterisation 13

3.2 Freestanding CNC films 17

3.3 Varying the evaporation rate of drop-cast CNC films 20

3.4 Improving the substrate's hydrophilicity 23

3.5 Strong magnetic field application in CNC film production 27

3.6 Electro-optical cell assembly using a freestanding CNC film 31

4 CONCLUSION AND FUTURE PERSPECTIVES 37

5 REFERENCES 41

6 SUPPORTING INFORMATION 45

6.1 AFM measurements of length and width of individual CNC particles 45

6.2 Evaporation rate depending on temperature 46

6.3 Specular and diffuse reflectance spectra for remaining films 47

6.4 SEM images used in the measuring of additional physical features 48

6.5 Videos displaying on and off cycles for the electro-optical cell 48

List of figures

FIGURE 1.1 – **A), B), C)** SCHEMATICS DEPICTING THE MOLECULAR ORDER OF A CRYSTALLINE STRUCTURE (SOLID), A LIQUID CRYSTAL AND AN ISOTROPIC STRUCTURE (LIQUID), RESPECTIVELY. **D), E), F)** DIFFERENT LIQUID CRYSTAL MOLECULAR SHAPES: CALAMITIC, DISCOTIC, AND BENT-CORE, RESPECTIVELY. 1

FIGURE 1.2 – **A)** SCHEMATIC REPRESENTATION OF A NEMATIC PHASE, WITH ITS DIRECTOR **N** POINTING UPWARD; **B)** SCHEMATIC DEPICTION OF A CHOLESTERIC PHASE, WHERE P/2 IS HALF THE LENGTH OF THE STRUCTURE'S PITCH. 3

FIGURE 1.3 – **A**) SCHEMATIC REPRESENTATION OF THE CHEMICAL STRUCTURE OF CELLOBIOSE, WHICH CONSTITUTES THE CELLULOSE MONOMER CELLULOSE. IT IS DIVIDED INTO TWO ANHYDROGLUCOPYRANOSE UNITS, CONNECTED BY THE SHOWN B-1,4 LINKAGE. **B)** AN ILLUSTRATION OF A CELLULOSE MICROFIBRIL, DIVIDED INTO AMORPHOUS AND CRYSTALLINE REGIONS. **C)** RESULTING CELLULOSE NANOCRYSTALS AFTER AN ACID HYDROLYSIS PROCESS COMPLETELY DISSOLVES AMORPHOUS REGIONS. ADAPTED FROM [15] WITH PERMISSION OF THE ROYAL SOCIETY OF CHEMISTRY. 4

FIGURE 3.1 – FTIR SPECTRA OF THE TWO DIFFERENT SAMPLES: MCC AND A CNC FILM. 13

FIGURE 3.2 – XRD DIFFRACTOGRAMS OF MCC AND CNC SAMPLES. 14

FIGURE 3.3 – AN AFM-CAPTURED IMAGE, IN AMPLITUDE RETRACE MODE, DISPLAYING A LARGE AMOUNT OF SCATTERED CNC PARTICLES. 15

FIGURE 3.4 – THERMAL ANALYSIS OF MICROCRYSTALLINE CELLULOSE AND CRYSTALLINE NANOCELLULOSE SAMPLES. 16

FIGURE 3.5 – **A)** PHOTOGRAPH OF PHASE SEPARATION OBSERVED BETWEEN CROSS POLARISERS IN SUSPENSIONS OF CELLULOSE NANOCRYSTALS WITH CNC CONTENT, FROM LEFT TO RIGHT, 2.8, 4.6, 7.5 AND 9.1 % (W/W); **B)** VOLUME FRACTION Φ OF CHOLESTERIC PLOTTED AS A FUNCTION OF THE CNC CONCENTRATION; POM IMAGES OF TEXTURES OBTAINED IN TRANSMISSION MODE FOR CNC SUSPENSION SAMPLES WITH C) 2.8 % (W/W), D) 7.5% (W/W), AND 9.1 % (W/W).SCALE BARS: **A)** 1 CM **C)** 100 MM; **D)** 50 MM; **E)** 20 MM. 17

FIGURE 3.6 – PHOTOGRAPHS OBTAINED THROUGH **A), B), C)** LCP LIGHT CHANNEL OF F1, F2, AND F3, RESPECTIVELY AND **D), E), F)** RCP CHANNEL LIGHT, AND F3, RESPECTIVELY. PHOTOGRAPHS WERE CAPTURED AT AN 8 ° ANGLE PERPENDICULARLY TO THE SUBSTRATE. SCALE BARS: 2 MM. 18

FIGURE 3.7 – **A), B), C)** POM REFLECTION IMAGES OF THE LCP LIGHT CHANNEL AT THE CENTRE OF F1, F2, AND F3, RESPECTIVELY; **D), E), F)** POM REFLECTION IMAGES OF THE RCP LIGHT CHANNEL AT THE CENTRE OF F1, F2, AND F3, RESPECTIVELY; **G), H), I)** LCP AND RCP REFLECTIVITY SPECTRA, MEASURED FOR WAVELENGTHS FROM 350 TO 800 NM, OF SAMPLES F1, F2, AND F3, RESPECTIVELY. SCALE BARS FOR **A) – F)**: 100 MM. 19

FIGURE 3.8 – PHOTOGRAPHS OF CNC FILMS **A), B), C)** T1, T2, AND T3 OBSERVED THROUGH UNPOLARISED WHITE LIGHT, RESPECTIVELY; **D), E)** T1 OBSERVED THROUGH LCP AND RCP LIGHT CHANNELS, RESPECTIVELY; **F), G)** T2 OBSERVED THROUGH LCP AND RCP LIGHT CHANNELS, RESPECTIVELY; **H), I)** T3 OBSERVED THROUGH LCP AND RCP LIGHT CHANNELS, RESPECTIVELY. PICTURES FROM D) TO I) WERE CROPPED IN HALF, AS TO BETTER INSPECT THE DIFFERENCE BETWEEN EACH CHANNEL. SCALE BARS: 1 MM. 20

FIGURE 3.9 – PROCESS OF EVAPORATION OF A DROP OF AQUEOUS SUSPENSION. ADAPTED BY PERMISSION FROM NATURE, LARSON, R. G. IN RETROSPECT: TWENTY YEARS OF DRYING DROPLETS. NATURE, 550(7677), 466-467., 2017. 21

FIGURE 3.10 – **A), B), C)** POM REFLECTION IMAGES OF THE LCP LIGHT CHANNEL AT THE CENTRE OF T1, T2, AND T3, RESPECTIVELY; **D), E), F)** POM REFLECTION IMAGES OF THE RCP CHANNEL AT THE CENTRE OF T1, T2, AND T3, RESPECTIVELY; **G), H), I)** LCP AND RCP REFLECTIVITY SPECTRA, MEASURED FOR WAVELENGTHS FROM 350 TO 800 NM, OF SAMPLES T1, T2, AND T3, RESPECTIVELY. SCALE BARS FOR **A) – F)**: 50 MM. 22

FIGURE 3.11 – PROFILOMETER SCANS ACROSS THE T1, T2 AND T3 SOLID FILMS OBTAINED FROM 2.8 % (W/W) CNC SUSPENSION DROPLETS ON ITO-COATED GLASS SUBSTRATES OBTAINED AT 3 °C, 22 °C, AND 60 °C, RESPECTIVELY. 23

FIGURE 3.12 – PLOTTED RESULTS OF AVERAGE STATIC CONTACT ANGLE MEASUREMENTS USING SESSILE WATER DROPLETS ON ITO-COATED GLASS SUBSTRATES FOR EACH CORRESPONDING AMOUNT OF EXPOSURE TIME. 24

FIGURE 3.13 – A), B), C) PHOTOGRAPHS OF U1, U2, AND U3 OBSERVED UNDER WHITE LIGHT; D), E) PHOTOGRAPHS OF U1'S LCP AND RCP LIGHT CHANNELS, RESPECTIVELY; F), G) PHOTOGRAPHS OF U2'S LCP AND RCP LIGHT CHANNELS, RESPECTIVELY; H), I) PHOTOGRAPHS OF U3'S LCP AND RCP LIGHT CHANNELS, RESPECTIVELY; J), K), L) PROFILOMETER SCANS OBTAINED ACROSS THE THREE FILMS SAMPLES. PICTURES FROM D) TO I) WERE CROPPED IN HALF, AS TO BETTER INSPECT THE DIFFERENCE BETWEEN EACH CHANNEL. SCALE BARS: 1 MM. 25

FIGURE 3.14 – **A), B), C)** POM REFLECTION IMAGES OF THE LCP CHANNEL AT THE CENTRE OF U1, U2, AND U3, RESPECTIVELY; **D), E), F)** POM REFLECTION IMAGES OF THE RCP LIGHT CHANNEL AT THE CENTRE OF U1, U2, AND U3, RESPECTIVELY; **G), H), I)** LCP AND RCP REFLECTIVITY SPECTRA, MEASURED FOR WAVELENGTHS FROM 350 TO 800 NM, OF SAMPLES U1, U2, AND U3, RESPECTIVELY. SCALE BARS FOR **A) – F)**: 50 MM. 26

FIGURE 3.15 – **A)** SCHEMATIC OF THE LIGHT'S COURSE WHEN THE CELL IS VIEWED FROM THE TOP OF THE DROP-CAST FILM. BOTH LCP AND RCP LIGHT ARE REFLECTED. **B), C)** LCP AND RCP LIGHT CHANNEL PHOTOGRAPHS, RESPECTIVELY. **D)** SCHEMATIC OF THE LIGHT'S COURSE WHEN THE CELL IS VIEWED FROM THE BASE OF THE DROP-CAST FILM. LCP LIGHT IS REFLECTED AND RCP LIGHT IS TRANSMITTED. **E), F)** LCP AND RCP LIGHT CHANNEL PHOTOGRAPHS, RESPECTIVELY. SCALE BARS FOR **B), C), E), F)**: 5 MM. 27

FIGURE 3.16 – SCHEMATIC OF HOW THE CHOLESTERIC LAYERS ARE ALIGNED IN THE CNC FILM, IN RELATION TO THE APPLIED MAGNETIC FIELD. THE MAGNETIC FIELD'S VECTOR (**B**) IS COLLINEAR WITH THE CHOLESTERIC AXIS (**Z**); BOTH ARE DIRECTED UPWARD. 28

FIGURE 3.17 – **A), B)** POM REFLECTION IMAGES OF THE LCP LIGHT CHANNEL AT THE CENTRE OF R1 AND R2, RESPECTIVELY; **C), D)** POM REFLECTION IMAGES OF THE RCP LIGHT CHANNEL AT THE CENTRE OF R1 AND R2, RESPECTIVELY; **E), F)** LCP AND RCP LIGHT REFLECTIVITY SPECTRA, MEASURED FOR WAVELENGTHS FROM 350 TO 800 NM, OF SAMPLES R1, R2, RESPECTIVELY. SCALE BARS FOR **A) – D)**: 50 MM. 29

FIGURE 3.18 – **A), B)** LCP LIGHT CHANNEL PHOTOGRAPHS OF R1 AND R2, RESPECTIVELY; **C), D)** RCP LIGHT CHANNEL PHOTOGRAPHS OF R1 AND R2, RESPECTIVELY. GLASS SUBSTRATES ARE PRESENT IN THE PICTURES, AS TO PREVENT THE FILMS FROM CURLING UP. PHOTOGRAPHS WERE TAKEN AT A 15° ANGLE PERPENDICULARLY TO THE SUBSTRATE. SCALE BARS: 2 MM. 29

FIGURE 3.19 – **A), B)** SPECULAR AND DIFFUSE REFLECTIVITY SPECTRA FOR R1 AND R2, RESPECTIVELY. SR STANDS FOR SPECULAR REFLECTIVITY, WHILE DR STANDS FOR DIFFUSE REFLECTIVITY. 30

FIGURE 3.20 – AFM-CAPTURED IMAGES OF A 20X20 MM SURFACE AREA OF R1 AND R2, IN AMPLITUDE RETRACE MODE. 31

FIGURE 3.21 – **A), B)** LCP AND RCP LIGHT CHANNEL PHOTOGRAPHS OF THE ELECTRO-OPTICAL CELL, RESPECTIVELY; **C), D)** LCP AND RCP LIGHT CHANNEL POM REFLECTION IMAGES, RESPECTIVELY, WHILE THE 5CB IS IN THE NEMATIC PHASE; **E)**, **F)** LCP AND RCP LIGHT CHANNEL POM REFLECTION IMAGES, RESPECTIVELY, WHILE THE 5CB IS IN THE ISOTROPIC PHASE. SCALE BARS FOR **A)**, **B)**: 2 MM. SCALE BARS FOR **C) – F)**. 32

FIGURE 3.22 – **A)** SEM IMAGE OF THE MICROGAP INSIDE THE CNC FILM. THE GAP EXTENDS FAR BEYOND THE SIDES OF THE IMAGE, IN REALITY, WITH VARYING GAP WIDTHS ALONG THE WAY. **B)** LCP AND RCP LIGHT REFLECTIVITY SPECTRA, MEASURED FOR WAVELENGTHS FROM 350 TO 800 NM, OF THE CENTRE OF THE ELECTRO-OPTICAL DEVICE. SPECTRA WERE NORMALIZED AROUND THE RCP LIGHT SPECTRUM. SCALE BAR FOR **A)**: 500 NM. 33

FIGURE 3.23 – SIMULATED REFLECTANCE SPECTRA BY MEANS OF A 4 × 4 BERREMAN MATRIX, FOR THE LCP AND RCP LIGHT CHANNELS, RESPECTIVELY. 34

FIGURE 3.24 – **A), B)** POM REFLECTION IMAGES OF THE LCP AND RCP LIGHT CHANNELS OF THE ELECTRO-OPTICAL CELL, RESPECTIVELY, WHILE IN THE OFF STATE. THE WIDE CHROMATIC GRADIENT IN **B)** CAN BE ATTRIBUTED TO OPTICAL INTERFERENCE FROM THE 5CB; **C), D)** POM IMAGES OF THE LCP AND RCP LIGHT CHANNELS OF THE ELECTRO-OPTICAL CELL, RESPECTIVELY, WHILE IN THE ON STATE. SCALE BARS:50 MM. 35

FIGURE 6.1 – A). B), C) EVAPORATION RATE GRAPHS FOR SAMPLES EVAPORATED AT 3 °C, 20 °C, AND 60 °C, RESPECTIVELY. EACH DIFFERENT SYMBOL REPRESENTS A DIFFERENT ARBITRARY SAMPLE, OUT OF A TOTAL OF 5 FOR EACH TESTED TEMPERATURE. 46

FIGURE 6.2 – **A), B), C)** SPECULAR AND DIFFUSE REFLECTIVITY SPECTRA FOR F1, F2, AND F3, RESPECTIVELY. IT IS CLEAR THAT, WHEN COMPARED TO SAMPLES R1 AND R2, THESE FILMS SHOWCASE A MUCH HIGHER DIFFUSE REFLECTIVITY RELATIVE TO THEIR SPECULAR REFLECTIVITY. SR STANDS FOR SPECULAR REFLECTIVITY, WHILE DR STANDS FOR DIFFUSE REFLECTIVITY..... 47

FIGURE 6.3 – SEM IMAGE OF THE FULL EXTENSION OF THE DROP-CAST FILM'S CROSSSECTION. SCALE BAR: 5 MM. 48

FIGURE 6.4 – SEM IMAGE OF THE FULL EXTENSION OF THE FREESTANDING CNC FILM'S CROSS-SECTION. ONE CAN IDENTIFY THE MICROGAP AS THE SMALL OPENING NEAR THE CENTRE. THE UPPER AND LOWER CHOLESTERIC LAYERS ARE ABOVE AND BELOW IT, RESPECTIVELY. SCALE BAR: 2 MM. 48

List of tables

TABLE 1 – CONCENTRATIONS, FILM THICKNESS, AND SUSPENSION VOLUMES ASSOCIATED WITH EACH OF THE STUDIED SAMPLES F1, F2 AND F3. 18

TABLE 2 – DATA ACQUIRED FROM FIGURE 3.19 **B)**. THE WAVELENGTH PEAK IS THE WAVELENGTH VALUE ASSOCIATED WITH EACH SPECTRUM'S MAXIMUM REFLECTIVITY VALUE, THE CALCULATED PITCH LENGTH IS THE EXTRAPOLATED CHOLESTERIC PITCH SIZE FROM EACH RESPECTIVE WAVELENGTH PEAK (USING THE DE VRIES EXPRESSION), AND THE SPECTRAL WIDTH IS EQUIVALENT TO FWHM VALUE OF EACH SPECTRUM. 33

Acronyms

5CB	4-pentyl-4′-cyanobiphenyl
AFM	Atomic Force Microscopy
ATR	Attenuated Total Reflectance
CNC	Cellulose Nanocrystal
CPDLC	Cellulose-based Polymer Dispersed Liquid Crystal
DR	Diffuse Reflectance
DSC	Differential Scanning Calorimetry
FTIR	Fourier-Transform Infrared
FWHM	Full Width at Half Measure
HPC	Hydroxypropyl Cellulose
ITO	Indium Tin Oxide
LCD	Liquid Crystal Display
LCP	Left Circularly Polarised
MCC	Microcrystalline Cellulose
NMR	Nuclear Magnetic Resonance
PVA	Polyvinyl Alcohol
POM	Polarised Optical Microscope
RCP	Right Circularly Polarised
RMS	Root Mean Square
SEM	Scanning Electron Microscope
SR	Specular Reflection
TGA	Thermogravimetric Analysis
UV	Ultraviolet
XRD	X Ray Diffraction

1 Introduction

1.1 Liquid crystals

It was Otto Lehmann who first reported the existence of these “mesomorphic states of matter”, in 1889, as he coined the terms “crystalline fluids” or “liquid crystals”. More than thirty years went by for these findings to be regarded as more than meets the eye by Georges Friedel. [1] Today, liquid crystals are present in various modern applications, but most prevalently in flat panel displays, commonly known as Liquid Crystal Displays (LCDs).

Liquid crystals were established as an intermediate state of matter, between isotropic liquids and crystals, separated by well-defined phase boundaries. Crystalline phase molecules tend to display precise spatial and orientational structuring, which might extend to a long range periodicity, in all three dimensions, whereas isotropic phase structures don’t display long-range organization at all. [1]

A defining feature of liquid crystals is their optical anisotropy, visible in the liquid crystalline state, which is manifested as birefringence. While an isotropic material (an isotropic fluid, for example) possesses only one refraction index, in an anisotropic medium (such as a solid crystal or a liquid crystal) it displays different refraction indexes depending on the direction of transmitted light. [2]

Different liquid crystalline compounds showcase varying degrees of positional order, which are subdivided into three main mesophases: the nematic phase is associated with no positional order, the smectic phase presents one dimensional positional order, and the columnar phase corresponds to a bidimensional positional order. [3] One other mesophase is acknowledged: the cholesteric phase, or chiral nematic phase, which is a subdivision of the nematic phase. [4] Depictions of these mesophases are presented in Figure 1.1.

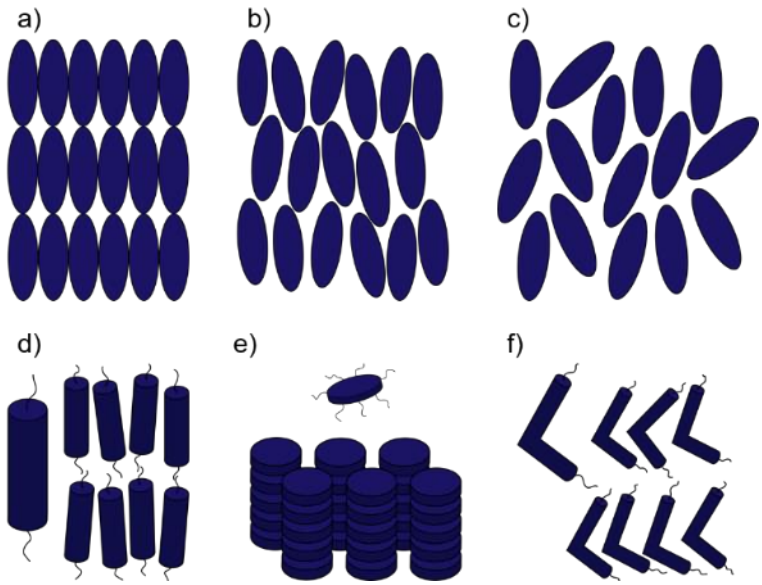

Figure 1.1 – **a), b), c)** Schematics depicting the molecular order of a crystalline structure (solid), a liquid crystal and an isotropic structure (liquid), respectively. **d), e), f)** Different liquid crystal molecular shapes: calamitic, discotic, and bent-core, respectively.

Liquid crystalline materials are also subdivided into thermotropic, lyotropic and barotropic natures, which determine the way they change phases. Regarding thermotropic substances, a transition between phases depends on a temperature variation, while lyotropic and barotropic phase shifts rely on concentration and pressure changes, respectively. [4], [5] The mesogenic molecules themselves also come in a variety of geometric shapes, the main ones being calamitic (rod-like), discotic (disc-shaped) and banana-shaped (with bent-cores), illustrated in Figure 1.1. [6]

In a liquid crystalline medium (as exemplified in Figure 1.1), the director **n** is defined as the vector indicating the average direction of the aligned elongated or flat molecules. Since, in reality, not all molecules point in the exact same direction, we can establish an arbitrary angle θ as the angle between the long axis of a single molecule and the director **n**. Thus, the observed orientational order can be described by a one order parameter $\langle S \rangle$:

$$\langle S \rangle = \langle \frac{1}{2} ([3\ cos^2\ \theta] - 1) \rangle \quad (1)$$

For a perfectly ordered state, with all molecules being completely aligned with each other and the director **n** (θ = 0 º), the equation resolves to $\langle S \rangle$=1. On the other hand, since in an isotropic medium all molecules are randomly oriented (each molecular axis points in all directions with equal probability), we end up with $\langle S \rangle$=0. [2]

1.1.1 Nematic liquid crystals

In nematic substances, though each molecule's centre of gravity is randomly positioned, a relative orientational order can be found among them. A single molecule's long range axis is strongly correlated with that of its neighbours which, in turn, is oriented on average with the mesophase's director **n** (Figure 1.2). This preferential alignment results in the optical anisotropy in a nematic: a light beam travelling perpendicularly to the director moves at a slower pace than one propagating parallel to the director. [4]

In the absence of external stimuli or specific anchoring from surfaces, the orientation of a nematic's director is randomly distributed. A surface alignment can be induced with a certain kind of anchoring (the main ones being planar, homeotropic and oblique anchoring) in order to produce a preferential direction of the nematic's director. Due to the broadness of the subject at hand, only planar anchoring regarding nematic liquid crystals will be approached, because of its relevance in this work. [1]

By using surfactants or physically rubbing a surface (under certain conditions), it is possible to induce a planar anchoring. When the liquid crystal molecules come into contact with this surface, they align tangentially to it. Additionally, due to the nematic's capabilities for long-range orientation, the alignment induced by the surface can, theoretically, propagate throughout the rest of the nematic liquid crystal. [1]

1.1.2 Chiral nematic liquid crystals

The cholesteric phase (or chiral nematic phase) is commonly formed by adding chiral dopants to a nematic liquid crystalline material. Its physical characteristics are mostly similar to the nematic phase, except for the fact that the molecules tend to align themselves in a helical shape, perpendicular to the director, as illustrated in Figure 1.2 **b)**. The length of a full rotation of the helix (360 º) is denominated as

the helical pitch (*P*). [7] These helical structures are responsible for a cholesteric material's iridescence, and its selective reflection depending on the incident light's wavelength and circular polarisation (iridescence is defined as variation of reflected wavelength based on the angle of incident light). [8] Similar structures have been described in multiple natural examples, such as in the exo-cuticles of certain species of beetles (*Plusiotis batesi*). [9]

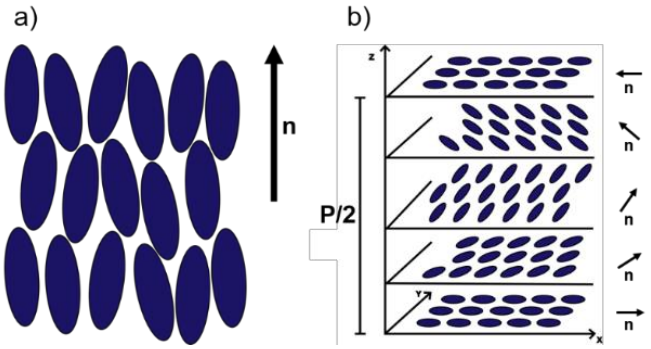

Figure 1.2 – **a)** Schematic representation of a nematic phase, with its director **n** pointing upward; **b)** Schematic depiction of a cholesteric phase, where P/2 is half the length of the structure's pitch.

Observation of a cholesteric structure reveals a reflected wavelength value (λ) which is dependent on the length of the helical pitch (P) and the average refraction index (n) according to de Vries expression (2) [10]:

$$\lambda = nP(sin\,\theta) \tag{2}$$

with θ being the angle between the incident light and the cholesteric layers. Therefore, at a normal angle of observation, the reflected light's wavelength is proportional to the cholesteric helical pitch. [11] The pitch length has been shown to be tuneable by external factors such as temperature and concentration. [12]

A chiral nematic material's intrinsic selective reflection depends on the handedness of the helix, as it can be either left-handed or right-handed. Assuming normal incidence, circularly polarised light with the same handedness of the helix is completely reflected, while an opposite handed circularly polarised light is completely transmitted. [7]

Cholesteric liquid crystals structures can be found in nature as in bacterial nucleoids, algae, cuticles of crustaceans and insects, bone, tendon, cornea, fish scales and scutes, plant cells walls and silk produced by spiders, just to name a few examples. [9], [13] If the cholesteric pitch is in the range of the wavelength of the visible light, vibrant colours can be observed. This so called structural coloration can generate a collection of complex optical effects ranging from iridescent and metallic colours, to brilliant white or black. [9]

1.2 Cellulose and its derivatives

Cellulose is the most abundant of all naturally occurring polymers and can be found in plant cell walls (in fibrillary form), some bacteria, algae and fungi. [14] Its monomer, cellobiose, is composed of two anhydroglucopyranose units twisted 180 º around a β-1,4 linkage (Figure 1.3 **a)**). Its versatility and outstanding bio-sustainability make it one of the most promising organic compounds in a wide variety of research and industrial areas. [14] There are at least four polymorphs (supramolecular arrangements) of crystalline cellulose, types I through IV. This thesis will focus on cellulose type I, which is naturally obtained from a multitude of organisms (tree, plants, bacteria). Its relevance to this work resides in the fact that, among its various derivatives, cellulose nanocrystals (CNC) can self-assemble into a cholesteric liquid crystalline phase, while suspended in water.

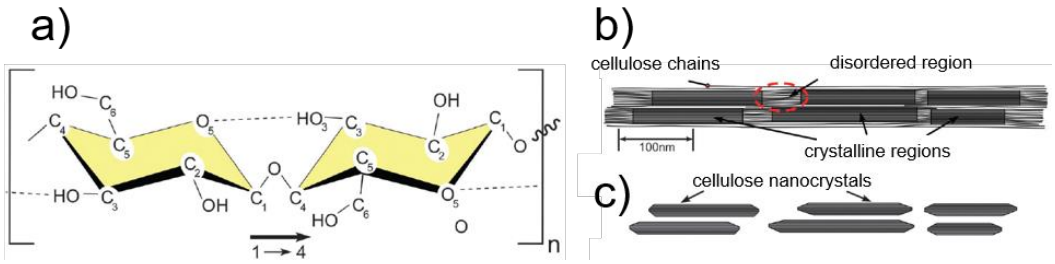

Figure 1.3 – **a**) Schematic representation of the chemical structure of cellobiose, which constitutes the cellulose monomer cellulose. It is divided into two anhydroglucopyranose units, connected by the shown β-1,4 linkage. **b)** An illustration of a cellulose microfibril, divided into amorphous and crystalline regions. **c)** Resulting cellulose nanocrystals after an acid hydrolysis process completely dissolves amorphous regions. Adapted from [15] with permission of The Royal Society of Chemistry.

Structurally, cellulose is constituted by a linear chain of cellobiose units, which are aggregated into larger microfibrils (5 – 20 μm of diameter). Within these microfibrils, formed from a bundle of nanofibrils (3 – 20 nm of diameter), the cellulose chains are regionally divided into either crystalline or amorphous domains (Figure 1.3 **b)**). The extraction of these crystalline regions, through chemical methods such as acid hydrolysis (which dissolves most of the amorphous regions), results in rod-like cellulose nanocrystals (Figure 1.3 **c)**). [15], [16] The exact dimensions of these crystals depend on the source of the cellulose and the reaction's conditions; a longer reaction time or increased acid concentrations lead to a decrease in both size and sample distribution. [17]

When suspended in water at low concentrations, CNCs form a left-handed lyotropic cholesteric phase. This mesophase is conjectured to be due to electrostatic stabilization conveyed by the CNC surface's negative charges introduced (after acid hydrolysis) by the sulphate ester groups. [9] A solid film can be produced from the suspension's full evaporation, in which the resulting pitch length can be short enough for the resulting photonic structure to reflect light in the visible spectrum. [18] This property enables the cholesteric suspension to be used as a template to produce structures with unique optical properties including iridescence and selective circularly polarised light reflection. Normally, this response is achieved in a so-called evaporation-induced self-assembly process. [9], [16] At a larger scale,

thin CNC films tend to display vast chromatic gradients, however, microscopically, their surface is populated by small and distinctly coloured domains, which are tied to different periodicities in cholesteric layering and pitch. [10]

The production of CNC films with uniform and controlled optical properties has been proven itself a notable challenge, due to the critical nature of controlling the liquid crystalline phase and its order across the drying process. In this process, the CNCs in suspension are initially in an isotropic (or biphasic) state, self-assembles to a fully cholesteric phase and finally to the solid state, via a glassy state or the kinetically arrested gel. In this glassy state, and due to the increased CNC concentration in the medium, the nanocrystals become sufficiently restricted in their ability to further relax, thus preventing any further cholesteric organization from occurring. [18] Regardless of the phase transition mechanism, should a sufficient amount of time be allocated the cholesteric phase can relax and reduce the probability of structural defects, giving rise to larger domains bearing uniform orientations. [16] From the numerous studies found in literature directed towards the control of optical properties of the CNC films, interesting results were ascertained relating to the fact that the morphology of the final solid structure is influenced by the suspension parameters and the conditions used in the solvent-casting method. These parameters include the CNC concentration on the suspension, the ionic strength of the CNCs, the suspension's exposure to magnetic field or electric field or shear fields, the drying rate of the solvent; the handedness to the LC mesophase correlated with the energy given to the system from using ultrasonic treatment, and the addition of another compound like glucose, PEG, or electrolytes.[9], [16], [19]–[29] Despite this myriad of studies around the production of CNC films, a consistent degree of control over its optical response and structure has still yet to be fully achieved.

1.3 Electro-optical devices and interactions with liquid crystals

Electro-optical devices span a plethora of different components and designs, all of which serving their own specific purpose. These devices can be used as high efficiency light shutters or as privacy windows since they can be electrically controlled to scatter light (off state) or to transmit it (on state). [30] This section will mostly focus on the introduction and functioning principles of electro-optical devices derived from cellulose-based systems, most like the one approached in this thesis.

In 1982, cellulose derivatives composites in electro-optical applications were initially introduced by Craighead et al. [31], followed a few years later by a different type of cellulose derivative electro-optical cell, called cellulose-based polymer dispersed liquid crystal (CPDLC). [32], [33] Due to the convenient match of both the nematic liquid crystal (E7) and HPC's refraction indexes (1.51 and 1.49, respectively), a very clear ON state is obtained when applying an electric field. The CPDLC cell was composed of a cellulose derivative polymeric film surrounded by two nematic layers sandwiched between two transparent electrically conductive substrates. These cells showed high transmission coefficients values (around 0.8) in the ON state, but their application capabilities suffered greatly from a high turn on field of around 1.5 V/μm, which led to exceedingly high turn-on voltages. [34]

More recently, a new type of electro-optical device with improved electro-optical properties was presented, while taking advantage of the high surface area of CNCs. Regarding this later technology, cellulose-based electro-optical devices were prepared by stacking, between two transparent conductive glass substrates, two layers of a nematic liquid crystal surrounding a thin CNC film. [35] This type of device allows for a major step forward in its functioning limitations by significantly reducing the turn on electric field and response time.

In the scope of the present work, the assembled electro-optical cell consists of a solid cholesteric CNC film sandwiched between two transparent electrodes. The electrodes are rubbed beforehand (as to induce a planar alignment in the nematic liquid crystal), and the device is filled with 4-pentyl-4′-cyanobiphenyl (5CB) and sealed. Should a micrometric gap form inside the CNC film during the evaporation process (as reported by *Fernandes et al.* [11]), the 5CB will infiltrate this space. This way, at an optical trajectory perpendicular to the substrates (and collinear with the CNC film's cholesteric helicoidal axis), it acts as a half-wave retardation plate, converting the handedness of the polarised light from left to right (Figure 1.4 **b)**). This mechanism allows for the device to reflect both LCP and RCP light. In the presence of an electric field, applied normally to the substrates, the nematic substance's director reorients itself to match the electric field's direction, thus reverting the electro-optical cell's optical properties to those of the CNC film, as is portrayed in Figure 1.4 **c)**. [11]

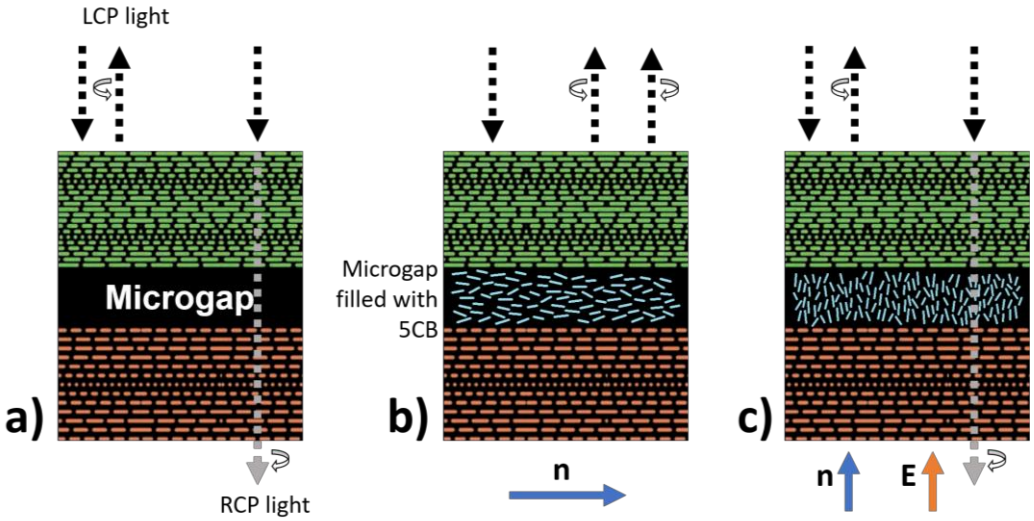

Figure 1.4 – Schematic of how light interacts with: **a)** a CNC film with no impregnated 5CB in its microgap; **b)** a CNC film with 5CB impregnated into its microgap, with a horizontal nematic director; **c)** a CNC film with 5CB impregnated into its microgap and an electric field pointing upward. Adapted from [11] with permission of John Wiley & Sons Inc, the Wiley Companies.

The formed nematic layer within the film should only behave as a half-wave retardation plate, when the phase difference produced between the ordinary and extraordinary rays (ΔΦ) is equal to π in the following equation (3):

$$\Delta\Phi = \frac{\Delta n\, d}{\lambda}\, 2\pi \tag{3}$$

Where Δn is the nematic crystal's birefringence value (equal to 0.3 for 5CB), d is the microgap's height, and λ is the wavelength of the incident light beam. [11]

A change in the nematic director's orientation is only observed above a certain applied external field threshold, beyond which, the transmissivity of the device gradually increases with the electric field. It is only at this point that the liquid crystal's elastic forces (strengthened by each substrate's induced planar anchoring) are overpowered by the external electric forces. This shift in orientation by an external electric field is called a Fréedericksz transition (depicted in **Erro! A origem da referência não foi encontrada.**). [36]

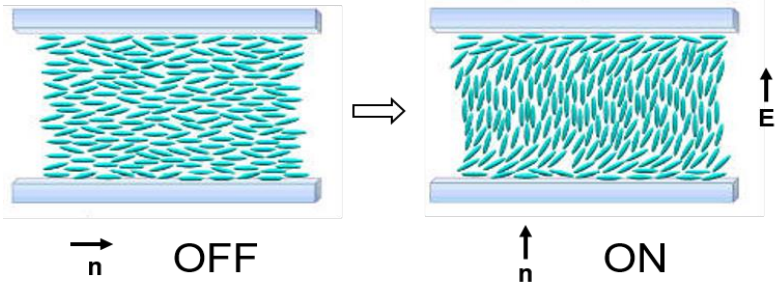

Figure 1.5 – A diagram of the Fréedericksz transition occurring in a nematic liquid crystal with positive dielectric anisotropy. As the electric field is turned on, directed upward, the nematic director aligns upward as well. Adapted from [60].

It is only due the 5CB's dielectric anisotropy that its director aligns parallel to the applied electric field's direction. Dielectric anisotropy can be either positive or negative, depending on the liquid crystal's molecular chemical structure. When these molecules have polar groups in their extremities, they carry permanent electric dipoles; when they don't, the molecules can rearrange themselves in order to originate induced dipoles. Depending on whether the dipole moment is either parallel or perpendicular to the molecule's most structurally organized axis, the molecules tend to align parallel or perpendicularly to the electric field's direction, respectively. A substance's dielectric anisotropy is positive when its director aligns with the electric field's direction (which is the case for 5CB); it's negative when its director is perpendicular to the applied field's orientation. [37]

The main focus of this dissertation was to explore, study and, ultimately, improve the optical response of CNC-based thin films, for further application in cellulose-based electro-optical devices. Multiple variables linked to the production of these CNC films were investigated as to increase LCP light reflectivity and extinguish RCP light reflectivity, while simultaneously aiming to control chromatic and structural homogeneity.

2 Materials and Methods

2.1 Production of CNC freestanding films and droplets

2.1.1 CNC production

Microcrystalline Cellulose (MCC; Avicel®, ~50 µm particle size, lot #BCBJ0229V), derived from cotton, was purchased from Sigma-Aldrich and sulfuric acid (95 %–97 % purity, Sigma-Aldrich) were used without further treatment.

The preparation of CNC particles was based on the documented method by *Gray et al.* [38], with small adaptations by *Fernandes et al.* [11]. Microcrystalline cellulose was hydrolysed in sulfuric acid (95 %, Sigma-Aldrich) with an acid/solid ratio of 8.5:1, at 45 ºC, for 130 minutes, while under continuous stirring. The resulting suspension was washed with ultrapure water in alternating stages of dilution and centrifugation (at 12 000 rpm for 20 minutes, using a Thermo Scientific Heraeus Multifuge X1R Centrifuge Series) until pH was raised to approximately 1.9–3.9, at which point the supernatant achieves turbidity and the suspension is collected. This resulting suspension was, in turn, placed into cellulose membranes (Spectrum Spectra/Por® 4 dialysis membranes) and dialyzed against ultrapure water (replaced daily for at least a month) until a constant pH was attained. The suspension was prepared with 3 consecutive cycles of 20 min of sonication over an ice bath using a Hielscher UP400S ultrasonic homogenizer (460 W, 24 kHz, at 0.85 of the cycle and 80% amplitude). Ultrapure water used in the process was purified using a Millipore Elix Advantage 3 water purification system.

The produced suspension was centrifuged and concentrated into an 11 % (w/w) aqueous CNC suspension, which in turn, was diluted into 4 other aqueous CNC suspensions, under different concentrations: 2.8 % (w/w), 4.6 % (w/w), 7.5 % (w/w), and 9.1 % (w/w).

2.1.2 CNC film production

Freestanding CNC films were produced by solvent evaporation method by depositing CNC suspension (at varying concentrations) onto polystyrene Petri dishes with 35 mm in diameter, under constant ambient conditions, until all the solvent evaporated (verified by constant weight). One freestanding CNC film was produced in the centre of a Bruker AVANCE III 300 MHz widebore solid state NMR with a continuous 7.05 T magnetic field applied perpendicular to the film's surface for the duration of the evaporation process.

CNC droplets were cast from a 2.8 % (w/w) aqueous CNC suspension with Easy 40+ micropipettes onto 100 Ω/□ Indium Tin Oxide (ITO)-coated square glass substrates (15x15x0.7 mm). Two replicas for each sample were produced and studied alongside the ones presented in this work. UV exposure of glass substrates was, when applicable, performed inside a Vilber Lourmat BLX-E254 UV-Crosslinker.

2.2 Electro-optical device assembly

Electro-optical cells were prepared by casting 40 µL of water/ethanol solution of polyvinyl alcohol (PVA) onto ITO-coated glass substrates' conductive side as to cover as much surface area as possible.

In order to induce a planar orientation onto the substrate, the PVA was carefully rubbed with broad, linear strokes, in a single direction (150 times for each substrate) using a velvet rag. An epoxy glue (Araldite ®) was mixed according to product instructions and a small portion was applied to four corners of one of the substrates. At this point, a small piece of CNC film was placed in the centre of the bottom substrate, and the top substrate was carefully set and lightly pressured on top of the glue drops. The substrates were overlapped in such a way that both substrates' planar orientations match in direction. The electro-optical devices were filled by capillarity with 4-pentyl-4′-cyanobiphenyl (5CB, K15 Licristal®, supplied by Merck). Electro-optical cells were sealed on all four sides with epoxy glue.

2.3 **Characterisation**

2.3.1 Chemical characterisation

Chemical characterisation via Fourier Transform Infrared (FTIR) spectroscopy was conducted on samples of microcrystalline and nanocrystalline cellulose. FTIR spectra were obtained using an attenuated total reflectance (ATR) sampling accessory (Smart iTR) equipped with a single-bounce diamond crystal on a Thermo Nicolet 6700 spectrometer. Spectra were acquired at 20 ºC, with data ranging from 4000 to 650 cm^{-1}, with a 4 cm^{-1} resolution. 32 scans were done, with an incident angle of 45 º.

2.3.2 Structural and dimensional characterisation

X-Ray Diffraction (XRD) curves were obtained using a PANalytical X'pert PRO model diffractometer, with Bragg-Brentano (θ/2θ coupled) geometry with graphite monochromated Cu KR (1.54 Å) radiation. Data was collected at a scanning step of 2θ=0.00334 º, from 10 º to 40 º.

Thermogravimetric analysis measurements (TGA) were performed using a Netzsch 449 F3 Jupiter® simultaneous thermal analyser. Each sample was heated from 25 to 550 ºC, at a heating rate of 5 ºC/min.

In order to topographically characterize the CNC films' surface, and measure the CNC particles' average length and width, Atomic Force Microscopy (AFM) data was acquired using an Asylum Research MFP-3D standalone system in tapping mode, with commercially available silicon AFM probes (scanning frequency of 300 kHz, k=26 N/m). The analysed CNC particles were prepared by casting 1 µL droplets of an ultra-diluted suspension of CNC in water (0.01 % w/w) onto a mica substrate (Muscovite Mica, V-5 from Electronic Microscopy Sciences). Immediately before deposition, the suspension was sonicated for two consecutive periods of 10 minutes (at 0.85 of the cycle and 80% amplitude).

Captured AFM images were analysed in Gwyddion software (version 2.50, http://gwyddion.net). The process of average dimensional distribution analysis consisted of 100 individual CNC particles' length and width manual measurements, while average surface roughness distribution was calculated automatically by the aforementioned software.

The thickness of freestanding CNC films, films from droplet casted onto glass substrate and electro-optical cells were estimated from at least 10 measurements (if possible) using a Mitutoyo digital micrometer.

Profilometry was used to map the surface of solid CNC films derived from droplets using a KLA Tencor D-600 stylus profilometer. Scanning speed was 0.05 mm/s, while stylus weight applied was 2 mg.

Further surface roughness analysis was performed on the CNC films, by means of total reflection and diffuse reflection, both obtained using a PerkinElmer Lambda 950 UV/VIS/NIR spectrometer. Specular reflection was extrapolated from these results.

Scanning Electron Microscopy (SEM) images of CNC films were acquired with a Carl Zeiss Auriga crossbeam (SEMFIB) workstation instrument equipped with an Oxford energy dispersive x-ray spectrometer. SEM images were captured in in-lens mode, with an acceleration voltage of 2 kV and an aperture size of 30 µm. Samples were glued onto aluminium substrates using a double-sided carbon tape and were coated with a thin carbon layer (<20 nm) using a Q300T D Quorum sputter coater.

2.3.3 Optical characterisation

All samples' photographs were taken with a Canon EOS 550D camera, equipped with a Canon EF-S 60mm Macro Lens.

Polarised Optical Microscopy (POM) images were observed using an Olympus BX-51 polarised optical microscope connected to an Olympus KL2500 LCD cold light source. LCP and RCP light images were observed using a quarter wave plate along with a linear polariser in the reflection's optical path. An equipped camera (Olympus DP73) and Olympus Stream Basic 1.9 software were used for image capture.

Spectrometer analysis of the produced CNC films and solid CNC films derived from droplets was measured with a Jobin Yvon H10 VIS monochromator mounted onto an Olympus BH2 optical microscope connected to an Olympus TH3 light source.

It is important to note that the POM images (from Olympus BX-51) and reflectance spectra (obtained while using the Olympus BH2) might not coincide exactly since it was not possible to guarantee that the same point of observation is used in both measures.

Contact angle characterisation was performed with a Dataphysics OCA 20 contact angle system supported by a dosing system with an attached needle measuring 0.69 mm in external diameter. Each substrate's water contact angle (static mode) was measured 10 times in non-overlapping regions, at room temperature, with each H_2O sessile drop being 5 µL in volume. Contact angle measurements were registered 5 seconds after each droplet deposition defined as the settled time.

3 Results and discussion

This dissertation's main goal was to optimize and reliably control distinguishing optical properties associated with thin solid films, obtained from solvent casting and evaporated of sessile cast droplets, prepared from anisotropic suspension of cellulose nanocrystals. The film's optical properties focused on this work are iridescence, selective reflection of left circularly polarised (LCP) light, and transmission of right circularly polarised (RCP) light. As such, several variables in the film production process were studied and correlated with the CNC films' optical features.

The studied factors include preparation of films from CNC suspensions with different CNC concentrations, evaporation temperatures of CNC droplets cast onto ITO-coated glass substrates, variation of ITO-coated substrate hydrophobicity and production of thin films while under the effect of a strong magnetic field. These points of study, mostly applied to CNC evaporated droplets used as a model, aimed to make CNC films thinner, more topographically homogeneous, and displaying improved optical responses. The film with the best optical properties was then impregnated with a nematic liquid crystal, 4-pentyl-4′-cyanobiphenyl (5CB), and assembled in an electro-optical cell. By application of electric field or temperature variation the birefringence of the liquid crystal could be tuned, and the reflected RCP light channel response observed.

3.1 CNC characterisation

CNC films, as well as the precursor CNC particles used in this work, were optically, chemically, morphologically, and structurally characterised. The films were studied using their respective central regions, unless otherwise noted. Assembled electro-optical cells were optically characterised.

Two FTIR spectra are shown in Figure 3.1, associated with MCC and an aqueous 2.5 % (w/w) CNC suspension.

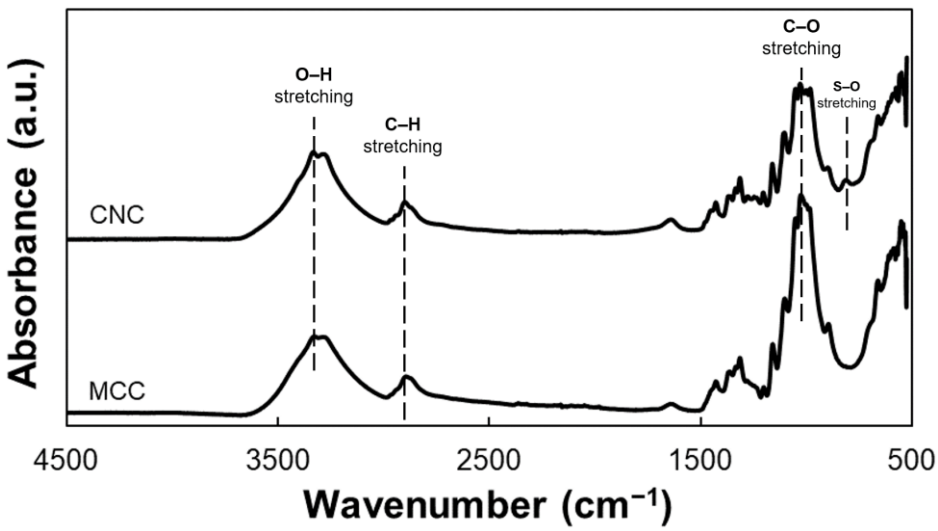

Figure 3.1 – FTIR spectra of the two different samples: MCC and a CNC film.

Both samples' spectra show the same cellulose characteristic peaks (O–H, C–H, and C–O stretching vibrations, at 3400 cm^{-1}, 2900 cm^{-1}, and 1060 cm^{-1}, respectively). Another peak, assigned to S–O bonds stretching, can be seen due to the presence of sulphate groups on the CNC sample at 817 cm^{-1}; this specific peak is absent on the MCC curve, since this sample did not suffer a hydrolysis process. [39]

In Figure 3.2, the two x-ray diffraction patterns belonging to MCC and CNC samples can be observed.

From the obtained diffractograms, one can identify the main peak (002) at around 2θ = 22.6 º, along with smaller overlapping peaks (101) and ($10\bar{1}$), at 2θ = 14.7 º and 16.8 º, respectively; these are characteristic peaks associated with cellulose type I, which confirms that the hydrolytic process does not affect the structural organization of the cellulose within the cellulose nanocrystals. The CNC diffractogram displays narrower and sharper peaks, due to its increased crystallinity, a consequence of the acid hydrolysis treatment. [40]

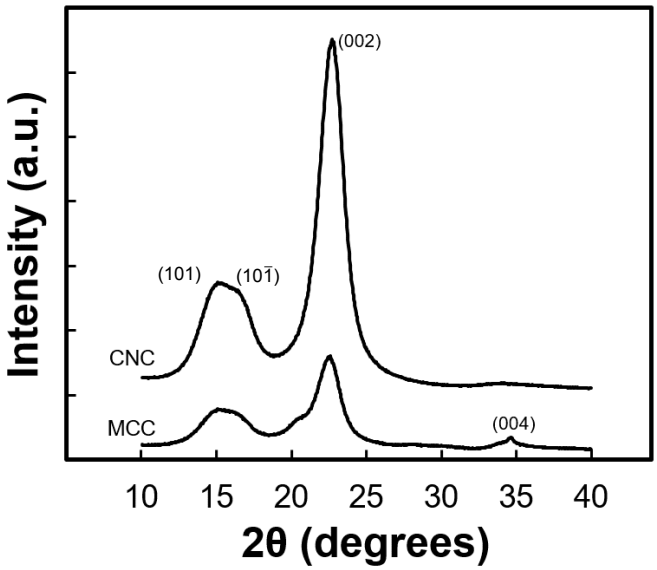

Figure 3.2 – XRD diffractograms of MCC and CNC samples.

The crystallinity index (I_C) was determined using the documented empirical method presented by *Segal et al.*. [41] Information extracted from Figure 3.2 can be used in the following equation (3):

$$I_c = \frac{I_{(002)} - I_{am}}{I_{(002)}} \times 100 \quad (3)$$

where $I_{(002)}$ is the maximum diffraction intensity of the (002) lattice peak at a 2θ angle between 21 º and 23 º. It represents the crystalline counterpart. $I_{(am)}$ is the intensity of diffraction of the amorphous material, taken at a 2θ angle between 18 º and 20 º, where the intensity is minimal. This calculation method is only valid as a comparison basis between samples.

MCC and CNC crystallinity indexes were calculated to be 76.19 % and 88.94 %, respectively. These values are in good accordance with literature [42], [43]

CNC particles were dimensionally characterised using Atomic Force Microscopy. Figure 3.3, below, shows an AFM-captured topographic image of dispersed CNC prepared from a 0.01 % (w/w) aqueous solution, after it has dried, where a rice-like shape can be observed.

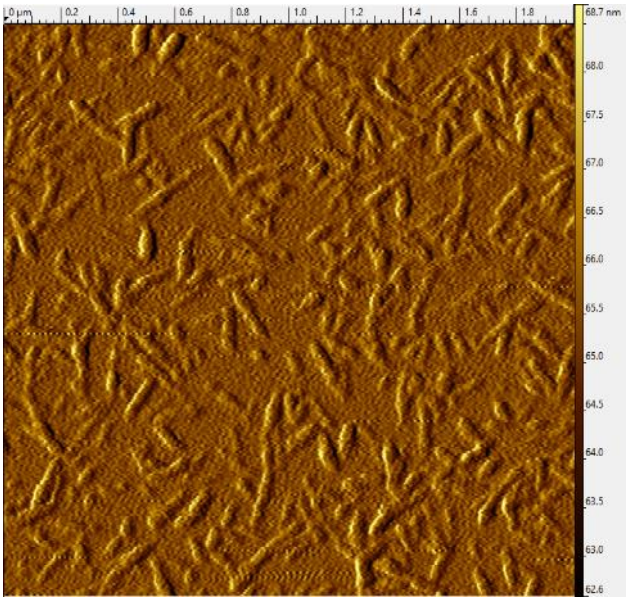

Figure 3.3 – An AFM-captured image, in amplitude retrace mode, displaying a large amount of scattered CNC particles.

CNC particle dimensions were obtained from 150 individual particle measurements on the AFM images and calculated to be, on average, 158 ± 37 nm long and 37 ± 10 nm wide. This equates to an approximate aspect ratio of 4.3:1. All registered measurements are presented in Supporting Information 1. While the average measured length of the particles is coherent with literature as reported by *Gaspar et al.* [42] (under similar hydrolysis conditions), the calculated width is marginally larger than what is expected (reported from 10 measurements from high-resolution SEM images) that might be related with the technique used in this study. Nevertheless, these results showed that the nanoparticles are obtained from the acid hydrolysis of microcrystalline cellulose (~ 50 µm as reported by the supplier).

Figure 3.4 shows the thermogravimetric and DSC curves (along with respective TGA curves) of two samples: the microcrystalline cellulose (MCC) Avicel® and the CNC produced by acid hydrolysis of MCC and CNC.

The MCC's TG curve shows the typical first-order reaction pyrolysis process of the cellulose [44] while the CNC's TG curve can be subdivided into two main events, as temperature rises. The first weight loss is observed from 50 ºC to 130 ºC and is attributed to a slight loss of mass that occurs in both samples, due to the evaporation of residual water contained in the samples. During the second event, from 150 ºC to 350 ºC, various degradation processes take place, including decomposition, dehydration

and depolymerisation of glycoside units. The CNC sample goes through this mass loss in two stages, since it underwent a hydrolysis process performed with H_2SO_4. The first stage (up to ~ 250 ºC) is associated with the degradation of regions more accessible to the sulphate groups, while the second one is understood to be the breakdown of the more crystalline regions of the sample, less affected by the hydrolysis process. On the other hand, the MCC sample's mass percentage takes an abrupt dive towards the end of this thermal interval. The final event, from 350 ºC onward, is linked to the oxidation and breakdown of the samples' carbon-based residues [42], [45]. Similar curves have been previously obtained by *Morais et al.*. [39]

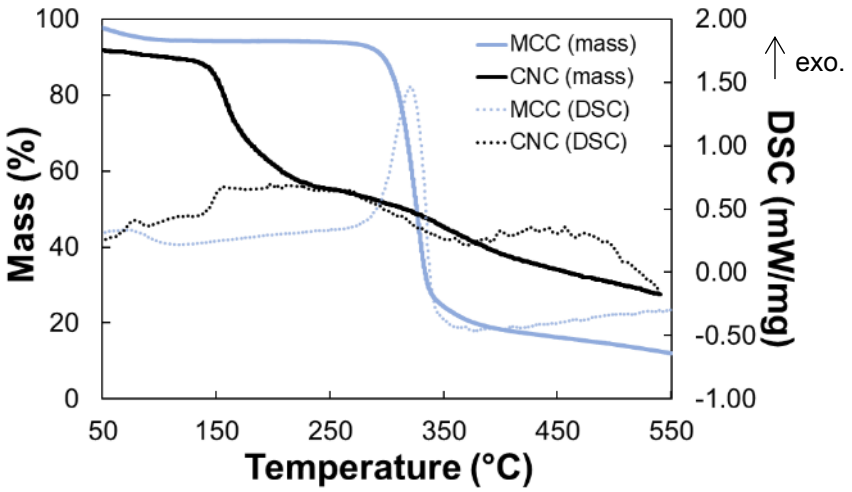

Figure 3.4 – Thermal analysis of microcrystalline cellulose and crystalline nanocellulose samples.

When CNC, obtained from acid hydrolysis, are suspended in a dilute aqueous solution, a single isotropic phase is formed due to the electrostatic repulsion experienced by the CNCs' overall negative charge density. If the concentration of CNC in suspension is increased, phase separation is observed and the sample is divided in two phases: cholesteric liquid crystal or anisotropic and isotropic. [46]. This macroscopic phase separation can be observed (Figure 3.5 **a)**) in our aqueous CNC suspensions with different content of nanocrystals.

Above a certain critical mass fraction (yet below the tested minimum of 2.8 % (w/w)), a small visible volume fraction of cholesteric liquid phase should begin to form at the bottom of the container, due to its higher density when compared to the isotropic phase. This volume fraction (Φ) of anisotropic phase (plotted in Figure 3.5 **b)**) rises gradually, but not linearly, as verified by *Lagerwall et al.* [22], until the observed fraction's phase becomes completely cholesteric, at a certain mass fraction between 7.5 and 9.1 % (w/w).

The POM image relating to the 2.8 % (w/w) suspension (Figure 3.5 **c)**) reveals a largely isotropic phase, identifiable by the visible black area of which the image is mostly comprised. Some cholesteric fingerprint textures can also be seen. The second sample, with a significantly higher CNC concentration (7.5 % (w/w)), showcases a great amount of tactoids and a visible decrease in isotropic regions (Figure

3.5 **d)**). The third and final sample (9.1 % (w/w), Figure 3.5 **e)**), while previously shown to be completely cholesteric at a macroscopic level, still exhibits minimal isotropic regions alongside more fingerprint textures. This should be attributed to the fact that, since the substance isn't perfectly homogeneous, a completely anisotropic phase is only attainable at relatively higher concentrations.

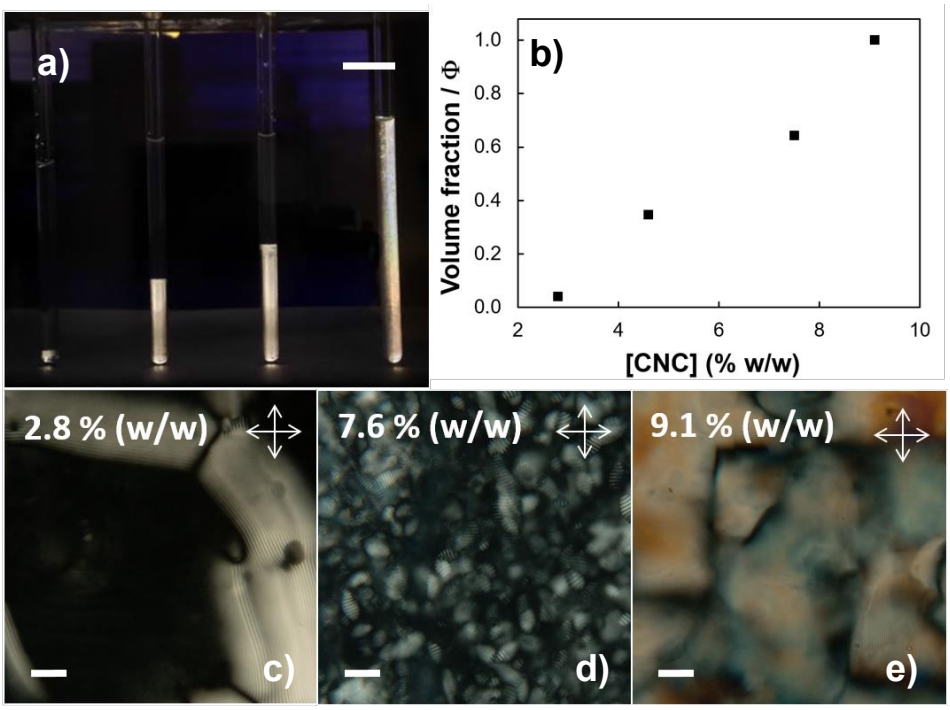

Figure 3.5 – **a)** Photograph of phase separation observed between cross polarisers in suspensions of cellulose nanocrystals with CNC content, from left to right, 2.8, 4.6, 7.5 and 9.1 % (w/w); **b)** Volume fraction Φ of cholesteric plotted as a function of the CNC concentration; POM images of textures obtained in transmission mode for CNC suspension samples with c) 2.8 % (w/w), d) 7.5% (w/w), and 9.1 % (w/w).Scale bars: **a)** 1 cm **c)** 100 µm; **d)** 50 µm; **e)** 20 µm.

3.2 **Freestanding CNC films**

By loosely following the presented phase diagram, aqueous CNC suspensions with varying concentrations of 2.8 %, 4.6 % and 6.1 % (w/w) were evaporated in polystyrene *Petri* dishes with 35 mm in diameter, at a constant temperature of 18 ºC, for approximately 15 days. The evaporation of this aqueous suspension give rise to iridescent chiral nematic films that reflect colours in the visible region of the electromagnetic spectra. The resulting freestanding films, referred to as F1, F2, and F3, respectively, are shown in Figure 3.6. Is important to note that the presented films evaporated from different volumes of suspension which consequently, varied their respective thickness. Physical data regarding the produced films is showcased in Table 1.

Table 1 – Concentrations, film thickness, and suspension volumes associated with each of the studied samples F1, F2 and F3.

Sample	[CNC] (% w/w)	Film thickness (µm)	Suspension volume (ml)
F1	2.8	147 ± 7	10
F2	4.6	43 ± 3	2
F3	6.1	72 ± 6	2

Each film's superficial features can be linked to the amount and concentration of suspension used to produce it. F1, comparatively to both its counterparts F2 and F3, exhibits the opaquest structure due to its thickness. Likewise, F2 and F3, using 2 ml of suspension, display a more translucid surface, with the former using a less concentrated suspension, which evidently leads to a smoother exterior. This is further illustrated in the comparison between F2 and F3's RCP channels (Figure 3.6, **e)** and **f)**): while both extinguish some percentage of reflected RCP light, the former does so more consistently and effectively.

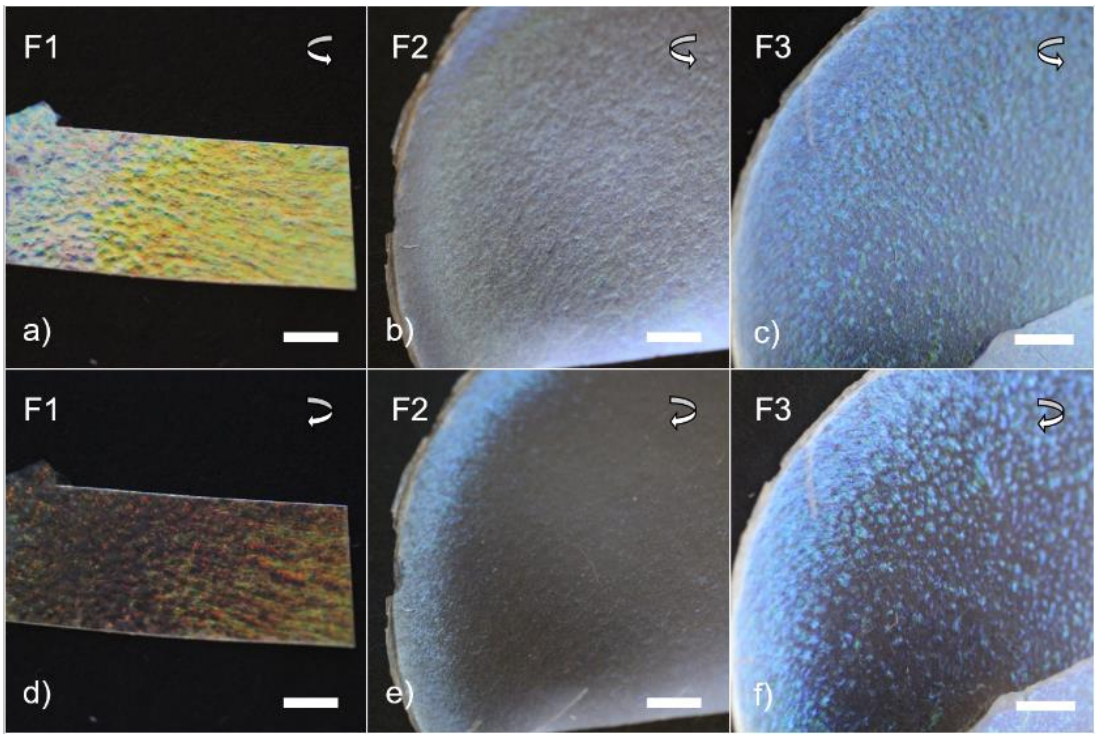

Figure 3.6 – Photographs obtained through **a), b), c)** LCP light channel of F1, F2, and F3, respectively and **d), e), f)** RCP channel light, and F3, respectively. Photographs were captured at an 8 º angle perpendicularly to the substrate. Scale bars: 2 mm.

Another noteworthy aspect to denote is each film's structural coloration. F1 displays vibrant yellow/red reflections, along with bright blue tones around its edges whereas, the remaining samples showcase a mostly blue surface. So, the film's reflection maximum wavelengths were shown to decrease as the CNC concentration in the precursor suspension increases, leading to a smaller average pitch length within the film's cholesteric layers. Similar correlation of cellulosic derivative concentration and reflecting

coloration has already been demonstrated by *Fernandes et al.* [47] for other cellulosic derivatives such as hydroxypropyl cellulose (HPC) while in aqueous solution. The authors demonstrated that HPC/H_2O solutions with 60 % (w/w) of HPC present a red wavelength reflection that is shifted to lower wavelengths as the concentration increases, resulting in a solution with a purple coloration at 65 % (w/w). The observation of F1 – F3 by optical microscopy with circularly polarised light and the spectra obtained for each observation (showed in Figure 3.7) are in good agreement to what is macroscopically observed. Assuming an ideal cholesteric structure along the entire vertical extension of the film, the RCP channel image should be perfectly black. All three samples, however, do reflect RCP light, as pictured in Figure 3.7, **d) – f)**, which is a main indicator of poorly organized cholesteric layers, both spatially and orientationally [48]. The films also display a vast array of colours in their LCP channel, further evidenced by large calculated spectral widths of ~ 200 nm for F2 and F3, and 158 nm for F1.

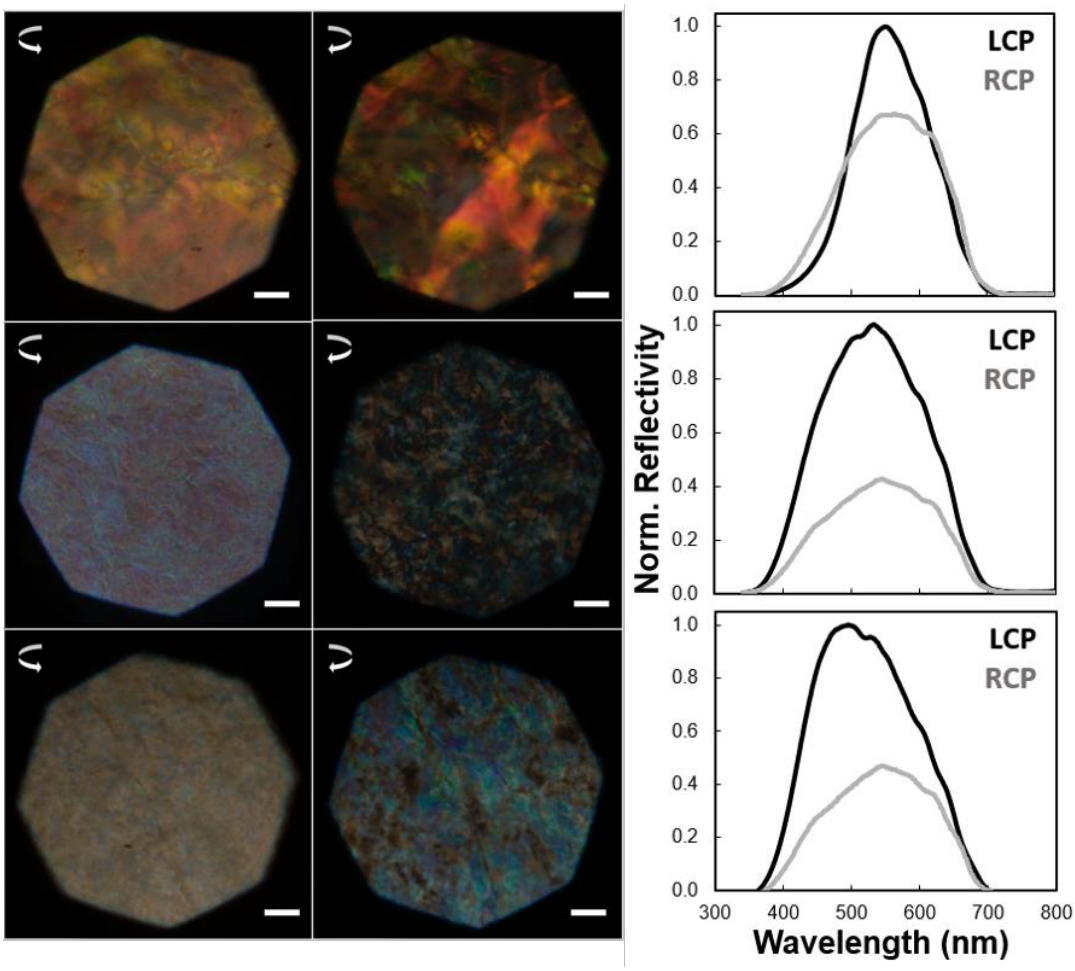

Figure 3.7 – **a), b), c)** POM reflection images of the LCP light channel at the centre of F1, F2, and F3, respectively; **d), e), f)** POM reflection images of the RCP light channel at the centre of F1, F2, and F3, respectively; **g), h), i)** LCP and RCP reflectivity spectra, measured for wavelengths from 350 to 800 nm, of samples F1, F2, and F3, respectively. Scale bars for **a) – f)**: 100 µm.

The spectral width of a LCP reflectivity curve is merely the Full Width at Half Maximum (FWHM) value for each peak. [48] A narrower FWHM value signifies a smaller spectral width, which in turn is

associated with a short amount of chromatic variance in the analysed reflected light. As such, a region with a narrow spectral width is expected to demonstrate a better cholesteric arrangement, with less physical and optical defects.

In the end, due to its low spectral width and vibrant macroscopic colours, an aqueous CNC concentration of 2.8 % (w/w) was determined to potentially provide optimal results in the future. Since a large amount of cellulose nanocrystals suspension is necessary to produced films, like the ones presented above, the study of different experimental conditions on films preparation was ascertained with sessile droplets cast onto the ITO-coated substrates, which are used in electro-optical cells.

3.3 Varying the evaporation rate of drop-cast CNC films

The solid films presented in Figure 3.8 were produced from 10 µL droplets of aqueous CNC suspension (2.8 % w/w) cast onto an ITO-coated glass substrate, which underwent complete evaporation at three different temperatures: 3 ºC, 22 ºC, and 60 ºC. From this point on, the films shall be denominated as T1, T2, and T3, respectively.

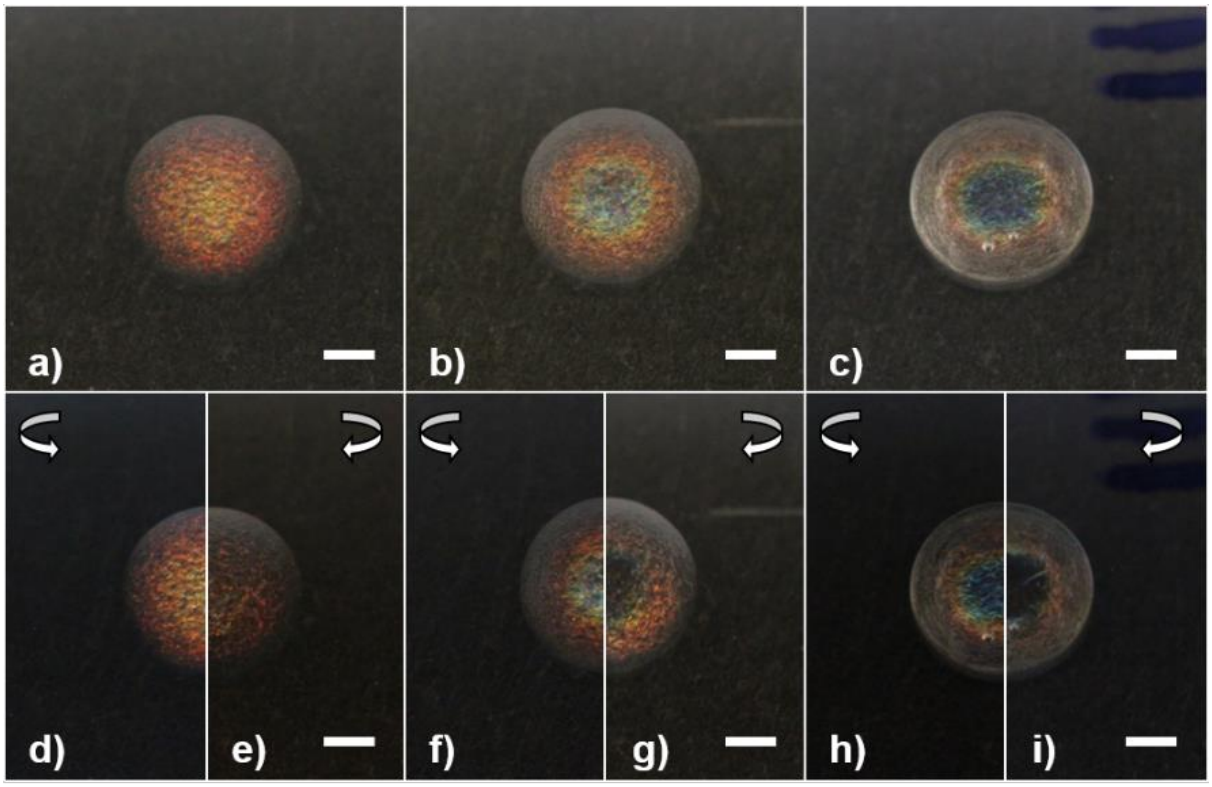

Figure 3.8 – Photographs of CNC films **a), b), c)** T1, T2, and T3 observed through unpolarised white light, respectively; **d), e)** T1 observed through LCP and RCP light channels, respectively; **f), g)** T2 observed through LCP and RCP light channels, respectively; **h), i)** T3 observed through LCP and RCP light channels, respectively. Pictures from d) to i) were cropped in half, as to better inspect the difference between each channel. Scale bars: 1 mm.

At a macroscopic scale, a heterogeneous colour pattern between the three samples can be identified, becoming more prevalent as the evaporation temperature increases (Figure 3.8 **a)** versus **c)**). T1's

central surface presents bright orange, which increases in wavelength to a deep red, as we move towards the film's edge. In sample T2, a similar pattern can be seen, but starting at the blue end of the spectrum, in the centre, and reaching red tones at the perimeter, where hints of uncoloured regions also begin to show. The remaining film, T3, displays a consistently blue central area, but the formed outer ring doesn't seem to reflect colour this time around.

Films produced from the evaporation of the sessile droplets at higher temperatures (T2 and T3) display what has been reported as the "coffee stain" effect. [19] This phenomenon, occurring in similarly cast CNC aqueous suspensions, consists of the appearance of a concentric ring along the outer edge of the circular droplet, chromatically and topologically different.

The coffee stain effect, first coined by Deegan et al. [49], is described as the migration of solids in a drying drop directed towards its outer edge, known as the contact line, thus forming a solid ring after full evaporation (Figure 3.9 **c)**). This occurs due to the existence of a pinned contact line, making the fluid flow outwards in order to compensate for evaporative losses. This way, evaporation rate at a point closer to the contact line is greater than that at the centre of the droplet (Figure 3.9 **a), b)**). [49]

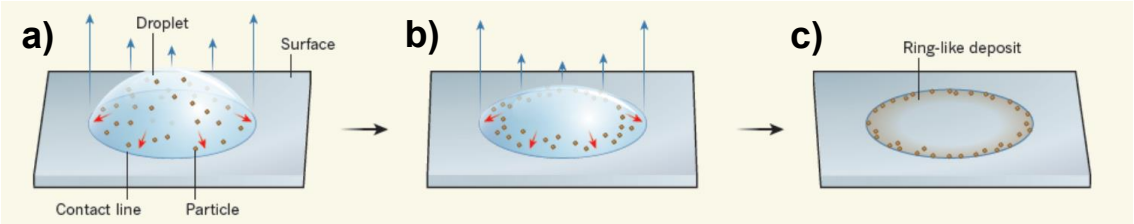

Figure 3.9 – Process of evaporation of a drop of aqueous suspension. Adapted by permission from Nature, Larson, R. G. In Retrospect: Twenty years of drying droplets. Nature, 550(7677), 466-467., 2017.

In this specific experiment, the concentric ring observed in T2 and T3 appears to increase in radius with temperature. Additionally, the film's iridescent properties falter in the mentioned region, as well as its reflective response to right circularly polarised light, both of which are potential symptoms of an unorganized chiral nematic structure. [48]

Each of the samples' different regions was analysed under a polarised optical microscope (Figure 3.10 **a)** – **f)**), in reflection mode. Captured images (Figure 3.10, **a)** – **f)**) are of each solid droplet's central region.

It was previously confirmed that, at a macroscopic level, T1 shows the most consistent optical response throughout its surface area (Figure 3.8 **a)**). However, T3's centre region does a better job at extinguishing RCP reflected light (Figure 3.10 **f)**), when compared to the same area in other samples (Figure 3.10 **d)** and **e)**). Additional evidence to support this comes from the region's LCP and RCP spectra (Figure 3.10 **i)**), where the RCP reflectivity band stands lower than the other samples' RCP peaks.

T3's LCP optical response (exclusively in its centre) is also noteworthy, as it is associated with the lesser of the three samples' spectral width (153 nm), implying that the measured region displays the most chromatically homogeneous reflection, nevertheless a dimmer colour is observed.

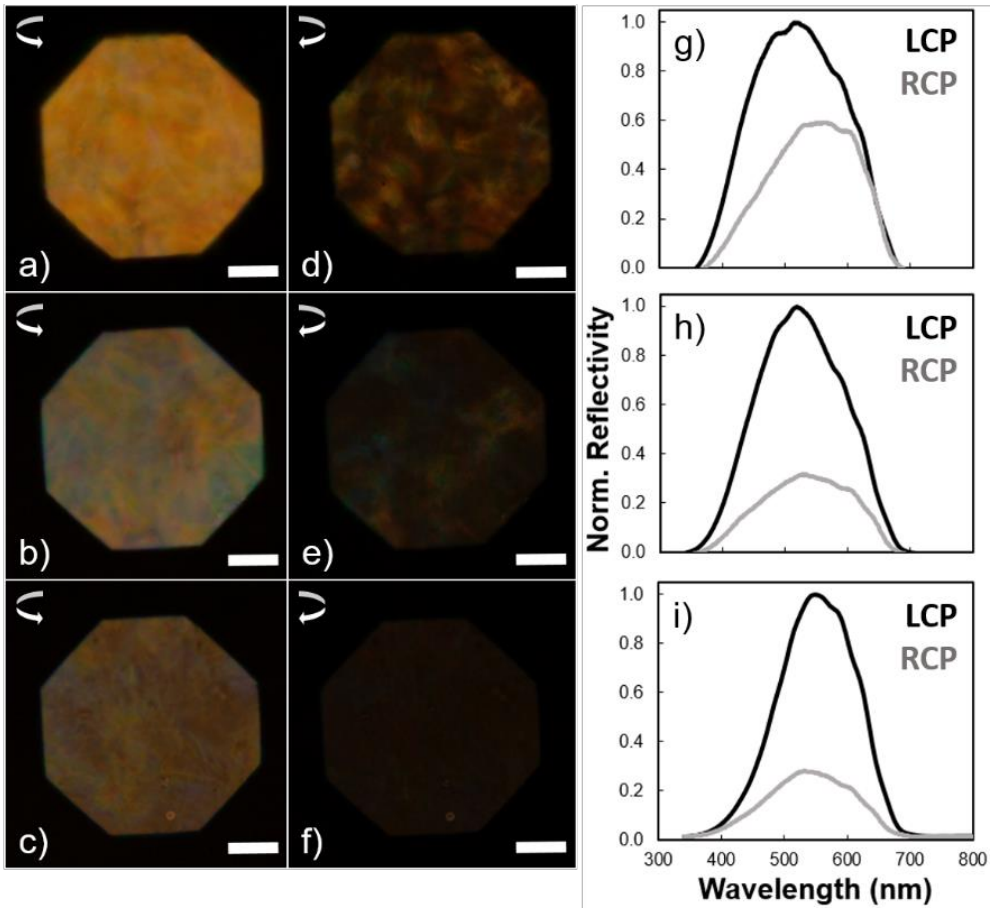

Figure 3.10 – **a), b), c)** POM reflection images of the LCP light channel at the centre of T1, T2, and T3, respectively; **d), e), f)** POM reflection images of the RCP channel at the centre of T1, T2, and T3, respectively; **g), h), i)** LCP and RCP reflectivity spectra, measured for wavelengths from 350 to 800 nm, of samples T1, T2, and T3, respectively. Scale bars for **a) – f)**: 50 µm.

Observed optical responses, which vary with film region and evaporation temperature, can be linked back to the "coffee-stain" effect. Although the cause for the coffee stain effect observed in droplets has yet to be correlated with thermal conditions during evaporation process, this demonstrated behaviour suggests that the coffee ring effect is lessened at lower temperatures of evaporation. One should stress that this correlation should not be necessarily related to the temperature of evaporation itself, but instead might be linked to the duration of the evaporation process, which is maximized at lower temperatures. In other words, as we decrease a droplet's temperature of evaporation, which in turn lowers its rate of evaporation, the droplet vaporizes at a more homogeneous pace, allowing for an even more flawless assembly along the cholesteric layers and fully dissipating the "coffee stain" effect. Alongside this experiment, a study on evaporation rate was performed for the three tested temperatures. From 50 µl droplets, average evaporation rate at 60 ºC was approximately 10 times faster than the rate at 3 ºC

(approximate rates of-1 mg/min vs. -0.1 mg/min). More details are available in Supporting Information 2.

Observed topography (Figure 3.11) matches reported results in literature [19] for T2 film, and aforementioned optical results. While T1 demonstrates a round surface, the other droplets show a concave surface (associated with the “coffee stain” effect). This physical manifestation becomes more prevalent at a higher evaporation rate (T3), and the particle build-up gradient between the centre and edges of the film becomes quite noticeable. In fact, the film thickness at the centre of T1 nearly quadruples relative to T3’s central section (40 μm vs. 10 μm). As such, one can argue that T3’s favourable LCP and RCP responses in its centre region might be merely linked to the evaporation process itself. An outward flow during the evaporation process should imply that the suspended particles at the centre of the evaporating drop-cast film are more still, while the ones closer to the contact line have a harder time relaxing. This way, cholesteric arrangement at the edges might be negatively affected; at the centre, on the other hand, it may be enhanced.

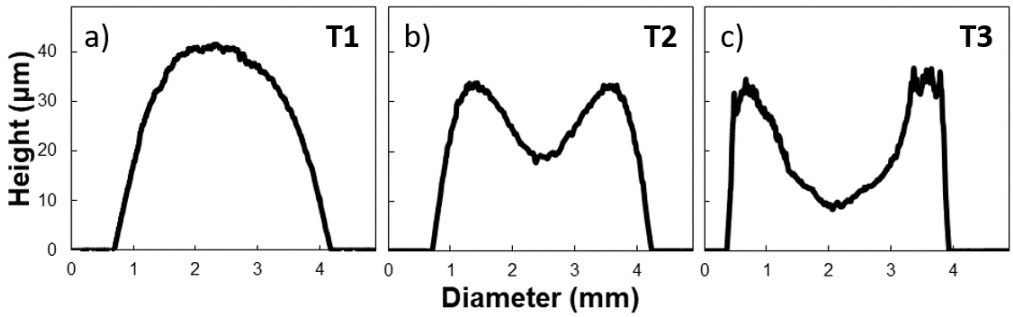

Figure 3.11 – Profilometer scans across the T1, T2 and T3 solid films obtained from 2.8 % (w/w) CNC suspension droplets on ITO-coated glass substrates obtained at 3 ºC, 22 ºC, and 60 ºC, respectively.

With that, the next step to optimize a CNC film’s optical response is to combine a slow evaporation process, which could grant the film its homogeneous colour and superficial structure, with a method to thin it even further.

3.4 Improving the substrate’s hydrophilicity

Results reviewed thus far indicate that CNC droplets evaporating at lower temperatures display better reflective and structural properties than those at higher temperatures. From this point forward, the variables were explored optimal droplet using an evaporation temperature of around 3 ºC, as established from previous conclusions.

Work focus shifted onto other potential film optimizations: reducing film thickness (while still aiming for a homogeneous surface) and further extinguishing of RCP reflected light. As such, in the interest of reducing film thickness, the substrate’s hydrophobic properties were investigated. In order to increase droplet spread on the ITO-coated glass substrate, which demonstrates high intrinsic hydrophobicity (with an average contact angle of ~ 107 ± 3 º was measured), the effects of prolonged exposure to ultraviolet (UV) radiation were tested with varying exposure intervals.

Extended exposure of UV light to hydrophilize various different solid surfaces has been extensively documented [51], [52]. Although specific research on the hydrophilization of ITO-coated glass substrates was not found, a simple 1 hour exposure test on such a substrate showed coherent results. UV radiation was chosen as a valid functionalization option since it does not measurably affect the ITO layer's electrical conductivity.

Static water contact angle analysis was performed on ITO-coated glass substrates exposed to UV radiation under differing amounts of time, from 0 to 8 hours. Results are displayed in Figure 3.12.

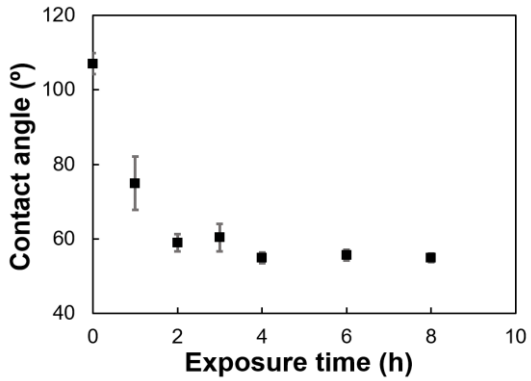

Figure 3.12 – Plotted results of average static contact angle measurements using sessile water droplets on ITO-coated glass substrates for each corresponding amount of exposure time.

It becomes clear that as exposure time increases, contact angle and (by extension) surface hydrophobicity both quickly decrease. This procedure seems to be most effective using exposure times of up to 2 hours (corresponding to a contact angle of ~ 60º), after which the average measured contact angle lowered only slightly, with up to 6 hours of additional exposure. Considering these results, three 10 µL droplets of CNC suspension were cast onto ITO-coated glass substrates, which were exposed to UV radiation for 1, 2, and 4 hours beforehand, and left to dry at 3 ºC. These samples will be referred to as U1, U2, and U3, respectively (Figure 3.13).

The films' reflected colours grow progressively fainter as UV exposure increases, since the same volume of material spreads along a larger area; however, for that same reason, RCP reflectivity tends to extinguish better as the hydrophobicity of the substrate decreases. Additionally, although a colour gradient is seen on all three samples, the profilometry data shows that this "coffee stain" effect does not extend to a topographic level. Sample U1 displays the most uniform of surfaces (Figure 3.13 **j)**), yet a clear change in reflected hues can be observed, gradually increasing in wavelength from its centre (blue) to its edges (red).

POM images (Figure 3.14) still feature a blend of blue, green and yellow colours (loosely comparable to T2 and T3's POM images in the same region (Figure 3.10 **b), c)**), derived from various spatial domains in the cholesteric layers. And even though U3 shows the best RCP response of the three samples (Figure 3.14 **f)**), by consistently reflecting very little light in that channel, it's suggested that this is (again)

linked to the lack of material in the observed area. This hypothesis is further supported by its abnormally high RCP reflectivity curve, in Figure 3.14 **i)**, which should indicate an already low LCP reflectance, in absolute terms.

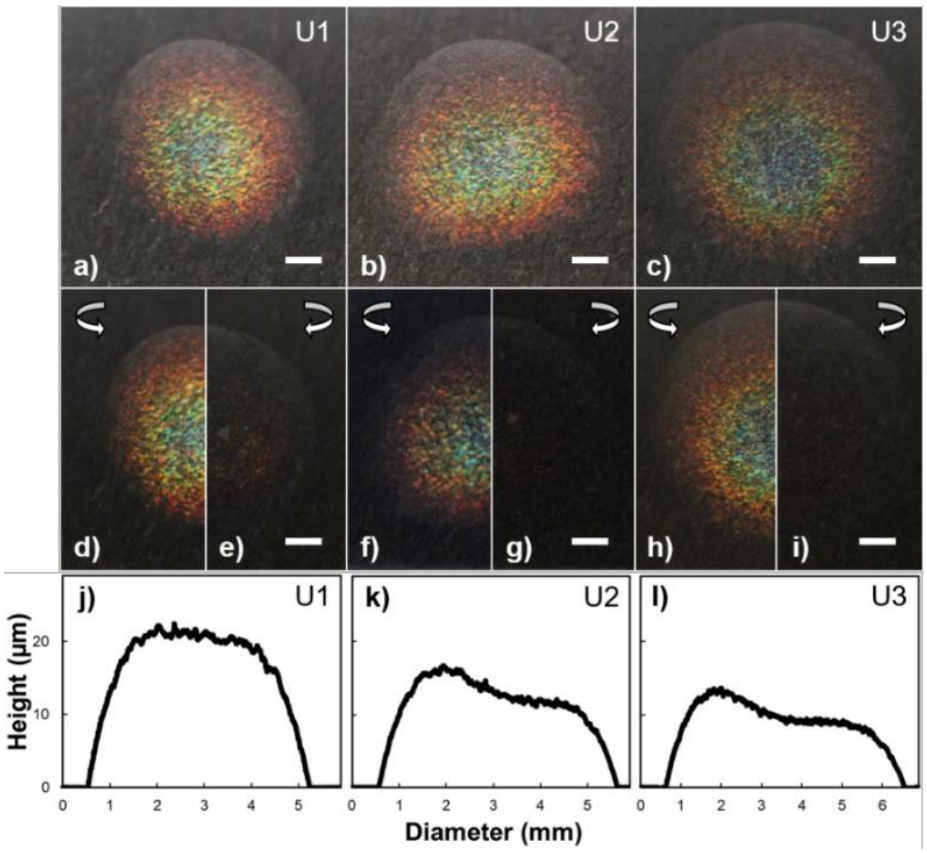

Figure 3.13 – a), b), c) Photographs of U1, U2, and U3 observed under white light; d), e) Photographs of U1's LCP and RCP light channels, respectively; f), g) Photographs of U2's LCP and RCP light channels, respectively; h), i) Photographs of U3's LCP and RCP light channels, respectively; j), k), l) Profilometer scans obtained across the three films samples. Pictures from d) to i) were cropped in half, as to better inspect the difference between each channel. Scale bars: 1 mm.

Out of these studied samples, U1 demonstrates the lowest relative reflectivity RCP light spectra (approximately 22 %), as well as the narrowest spectral width in the LCP light channel (162 nm), only slightly wider than that of T3 (153 nm). All while maintaining a reasonably homogenous superficial topography (Figure 3.13 **j)**).

In conclusion, a droplet of a CNC aqueous suspension, undergoing a very slow evaporation process on a hydrophilic surface, yields a solid film bearing significant optical and morphological improvements. However, although the original intent of forming CNC films from a sessile droplet was to significantly reduce material resource usage, as well as preparation time, these results showcase the limitations of the method itself. The final, optimized film still features a prominently round surface and a noticeable colour gradient, both of which disrupt a necessary degree of superficial homogeneity at such a small scale. Nonetheless, an attempt was made at incorporating a similarly produced drop-cast CNC film into an electro-optical device.

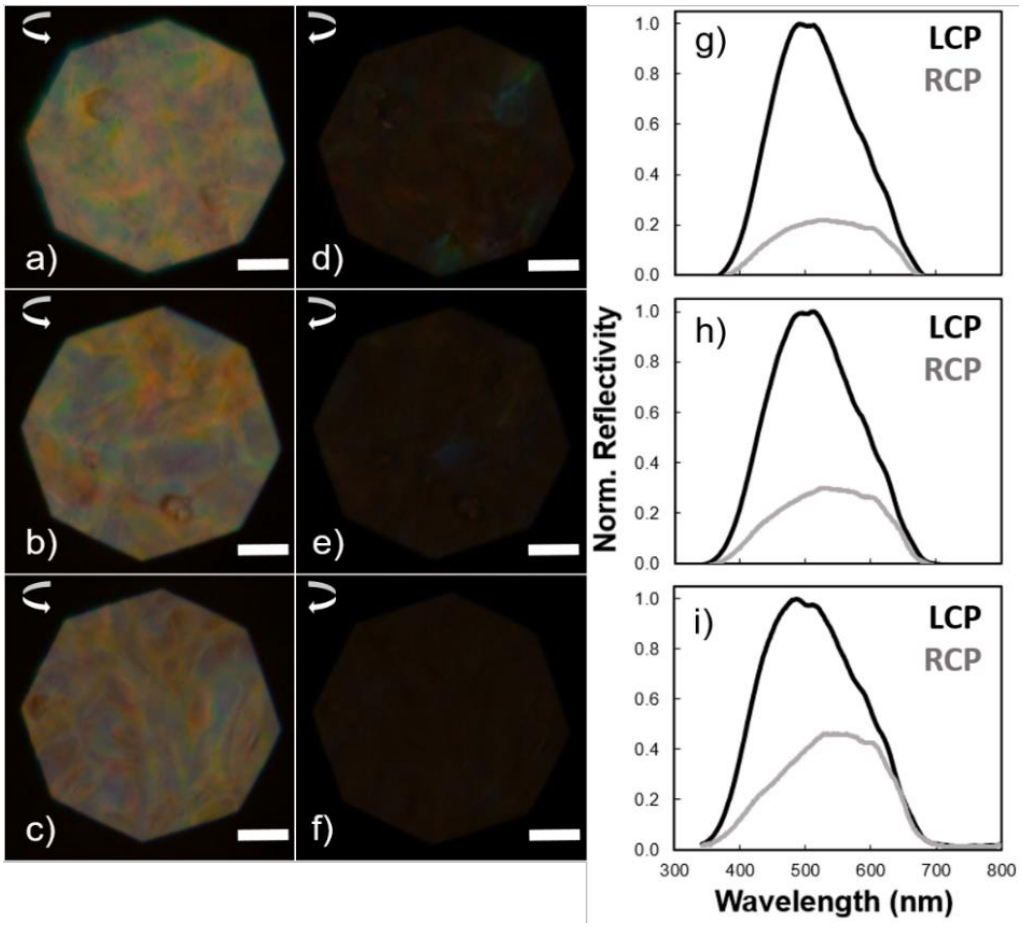

Figure 3.14 – **a), b), c)** POM reflection images of the LCP channel at the centre of U1, U2, and U3, respectively; **d), e), f)** POM reflection images of the RCP light channel at the centre of U1, U2, and U3, respectively; **g), h), i)** LCP and RCP reflectivity spectra, measured for wavelengths from 350 to 800 nm, of samples U1, U2, and U3, respectively. Scale bars for **a) – f)**: 50 µm.

3.4.1 Electro-optical cell assembly using a drop-cast CNC film

A CNC aqueous suspension droplet (50 µL) was drop-cast onto an ITO-coated glass substrate (previously treated with 1 hour of UV exposure) and fully evaporated at 3° C. The rest of the device was subsequently assembled as described in the Materials and Methods section.

The electro-optical device's optical response in the LCP and RCP light channels was observed macroscopically. When viewed perpendicular to the substrates, directly looking at the top side of the film, the cell reflects both LCP and RCP light (Figure 3.15 **a)**). However, when viewed from the opposite side, the cell reflects only LCP light; RCP light is transmitted (Figure 3.15 **d)**).

Observation of a cross-section of an identical drop-cast CNC film, by means of SEM, yielded no images of a visible microscopic gap within its cholesteric layers. However, the top section of the film was slightly damaged, as can be seen in Supporting Information 4, Figure 6.3. Nevertheless, the film's

reflection of both LCP and RCP light, as illustrated in Figure 3.15 **a)**, may only be occur when the nematic LC (5CB) infiltrates the film's microgap and acts as a half-wave retardation plate. Thus, it is possible that the expected microgap is indeed present, but situated very close to the top side of the drop-cast film. This way, when incident light hits the device from the film's top side (Figure 3.15 **a)**), the thinner upper layer and the thicker lower layers both reflect LCP and RCP light; however, when considering the other side, only the thicker upper layer reflects LCP light, while the thinner lower layer transmits RCP light.

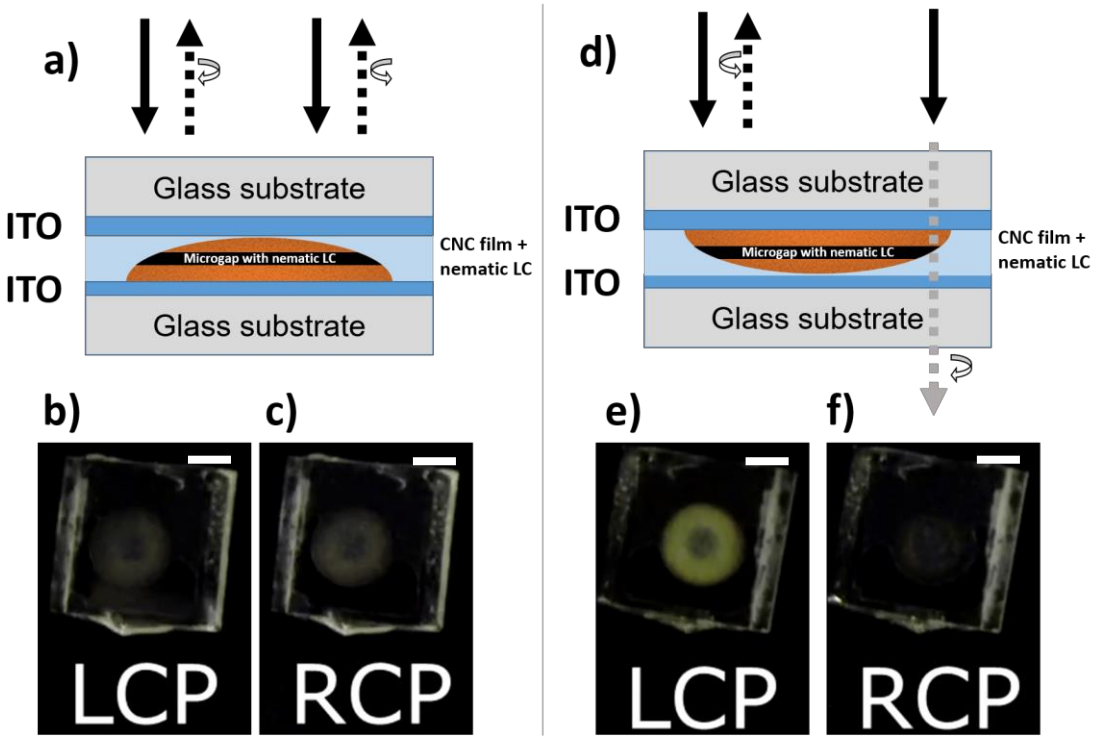

Figure 3.15 – **a)** Schematic of the light's course when the cell is viewed from the top of the drop-cast film. Both LCP and RCP light are reflected. **b), c)** LCP and RCP light channel photographs, respectively. **d)** Schematic of the light's course when the cell is viewed from the base of the drop-cast film. LCP light is reflected and RCP light is transmitted. **e), f)** LCP and RCP light channel photographs, respectively. Scale bars for **b), c), e), f)**: 5 mm.

Due to the lack of evidence of a microgap's existence, the production process of larger freestanding films was reapproached, focusing on reducing film thickness and optimizing cholesteric organization.

3.5 Strong magnetic field application in CNC film production

Two thin CNC membranes were produced from the deposition of 1 ml of 2.8 % (w/w) CNC aqueous suspension into polystyrene *Petri* dishes (diameter 35 mm). This amount was found to be the minimum required to keep the cast suspensions' surface tensions from breaking up, due to the substrates' hydrophobic properties, as one of the goals of this study is to minimize the resulting films' thickness.

While both films evaporated at 18 ºC, one of them did so while a continuous 7.05 T magnetic field was applied, perpendicular to the film's surface (Figure 3.16). This film will be referred to as R2, while

the other one will be designated as R1. These freestanding films' thickness values were found to be outstandingly thin, and measured to be 14 ± 3 µm and 16 ± 2 µm, respectively, for R1 and R2.

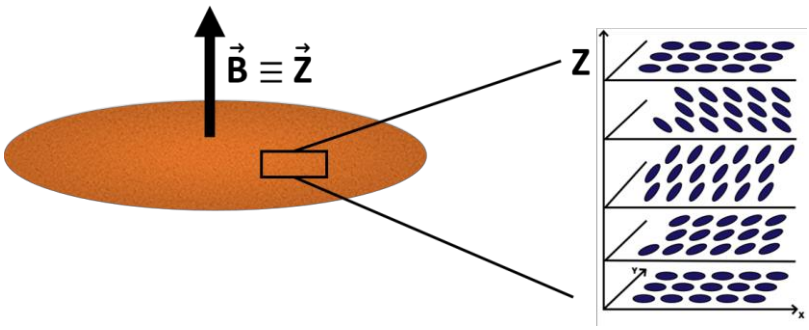

Figure 3.16 – Schematic of how the cholesteric layers are aligned in the CNC film, in relation to the applied magnetic field. The magnetic field's vector (**B**) is collinear with the cholesteric axis (**Z**); both are di-

The application of a relatively low (~ 0.5 – 1.2 T) external magnetic field to successfully influence the orientation of a CNC film's cholesteric domains, as it evaporates, has previously been reported by *Frka-Petesic et al.* [24]. In the presented study, a film assembled in the presence of a vertical magnetic field displayed a strong specular reflection in the direction perpendicular to the film's surface, indicating good alignment of the cholesteric structure according to the external field's directing vector.

R1 displays a vast array of colours, from blue to orange, depending on the observed region, while observed through LCP light (Figure 3.18 **a**). The film transmits RCP light relatively well, but this behaviour is gradually weakened as observation progresses towards its edges (Figure 3.18 **c)**). Its surface seems smoother than its predecessor (F1, Figure 3.6 **a)**), especially in its central region, as the edges are visibly rougher. A series of small dark spots populate its surface, although microscopic observation might determine their cause.

R2, unlike its counterpart, reflects a majority of red and orange hues along its surface while observed through LCP light (Figure 3.18 **b)**). Its RCP response is near-perfect, at a macroscopic level, only dwindling slightly around the very edge of the film (Figure 3.18 **d)**). Surface-wise, even though it is hard to tell from the captured images, R2 has a very polished metal-like surface unlike any other of the films produced so far. Unfortunately, as evidenced in Figure 3.18 **d)**, a small amount of dust settled into the suspension as it evaporated. Comparing its LCP and RCP light channel photographs, we can conclude that these specs of dust may be responsible for some of the film's chromatic disparities.

At a microscopic level, a significant difference can be ascertained between the two samples' central regions (Figure 3.17 **a), b)**). R1's LCP light channel displays a multitude of different colours (Figure 3.17 **a)**), as it did macroscopically, along what can be described as a flowing pattern, which may be linked to evaporation process as observed by *Dumanli et al.* [10]. On the other hand, R2's LCP channel exhibits remarkably consistent colour patterns (Figure 3.17 **b)**), varying only between few shades of orange. Albeit, their differences end there, as both films reflect little to no RCP light (Figure 3.17 **c)** and **d)**).

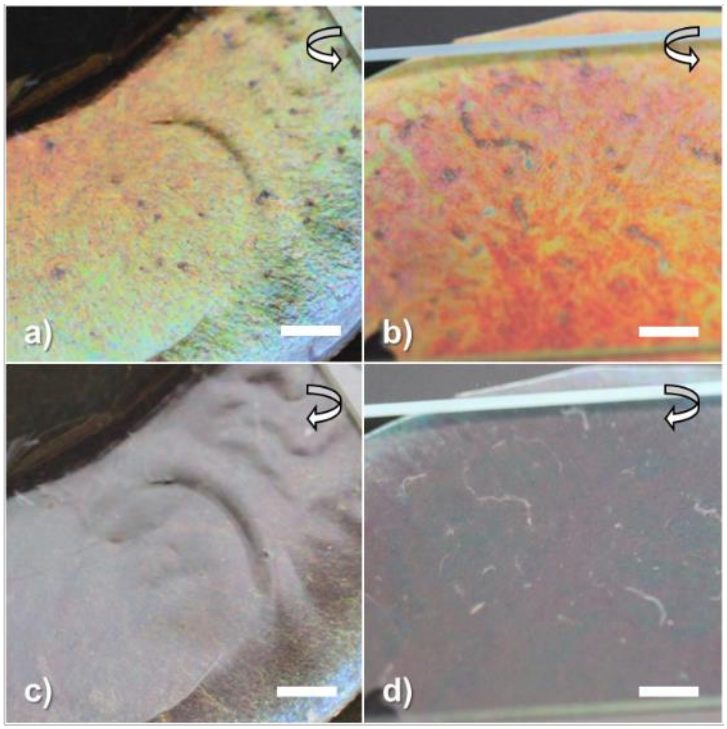

Figure 3.18 – **a), b)** LCP light channel photographs of R1 and R2, respectively; **c), d)** RCP light channel photographs of R1 and R2, respectively. Glass substrates are present in the pictures, as to prevent the films from curling up. Photographs were taken at a 15º angle perpendicularly to the substrate. Scale bars: 2 mm.

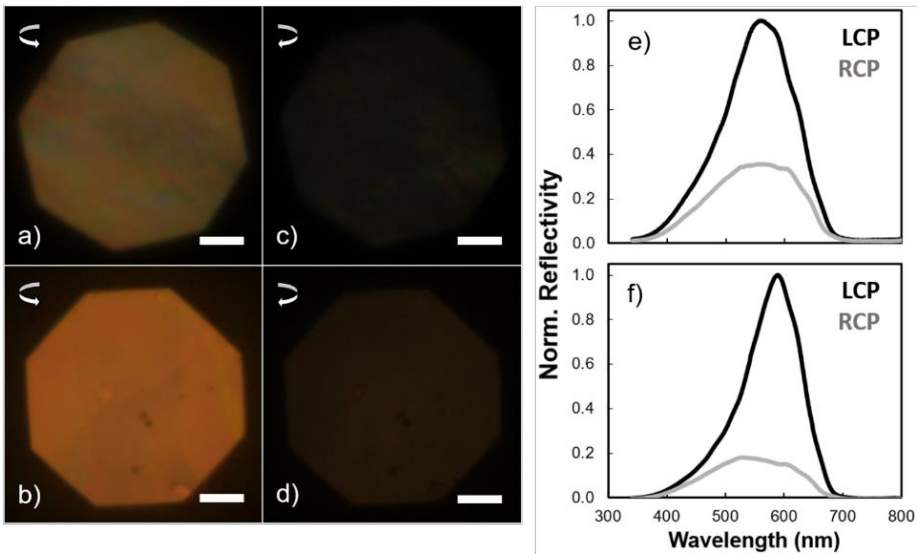

Figure 3.17 – **a), b)** POM reflection images of the LCP light channel at the centre of R1 and R2, respectively; **c), d)** POM reflection images of the RCP light channel at the centre of R1 and R2, respectively; **e), f)** LCP and RCP light reflectivity spectra, measured for wavelengths from 350 to 800 nm, of samples R1, R2, respectively. Scale bars for **a) – d)**: 50 µm.

The change in texture, from one sample to the other, suggests a direct correlation to the strong magnetic field's influence during R2's evaporation process. The orientation of cholesteric suspensions while under the influence of magnetic fields is owed to the individual CNCs' characteristic anisotropic diamagnetic susceptibility [53], an intrinsic property that leads to a cooperative effort in their cholesteric assembly process. [54] Due to the magnetic field's effects, the film's cholesteric helix axis tends to align vertically (with the external field's directing vector), perpendicularly to the substrate. Thus, during evaporation, the resulting cholesteric layers freeze with little to no visible tactoids, which lead to a more consistent colour scheme.

Reflectance analysis ((Figure 3.19, **e)** and **f)**) reveals a very narrow LCP spectral width measured on R2's surface (105 nm), along with R1's significantly larger spectral width of 142 nm. This is a fundamentally expected result, mainly due to R2's outstanding lack of optical defects and vibrant orange tones, which in turn are consistent with the measured maximum wavelength reflection peak at ~ 600 nm.

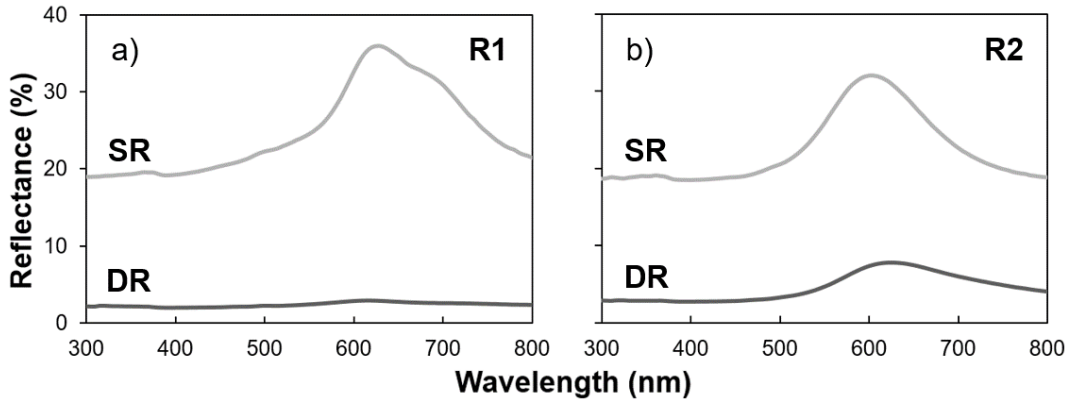

Figure 3.19 – **a), b)** Specular and diffuse reflectivity spectra for R1 and R2, respectively. SR stands for specular reflectivity, while DR stands for diffuse reflectivity.

In order to try understanding the origin of the metallic-like optical property observed specially in R2, the surface roughness of each film was analysed by two different characterisation techniques. Specular/diffuse reflectance analysis should quantify the membranes' long-range asperity, while AFM was used to fully assess their short-range average roughness.

Total reflectance is mainly divided into two components: specular and diffuse reflectance (SR and DR, respectively). The amount of diffused light, as it reflects off a sample's surface, should rise as its surface roughness increases; the opposite happens with the amount of specularly reflected light: it diminishes as surface roughness increases. Adapting this concept, by shining a light off a flat CNC film and measuring its total and diffuse reflection, one can extrapolate the amount of specularly reflected light, along a wide interval of wavelengths. Thus, when comparing each sample's specular and diffuse spectra, one can estimate a relative roughness index among tested films.

Both R1 and R2's diffuse reflection curves are well below their specular counterparts (Figure 3.19), indicating very low roughness. However, R2's diffuse reflectivity spectrum shows a slight peak, which is nearly undetectable in the former sample's spectrum. This could possibly be associated with the specs of dust embedded within R2, which may artificially increase the reflected light's diffuse component. The same characterisation process was performed on previously produced films (F1, F2, F3), and all of which showcased a significantly higher diffuse reflectivity spectrum. A summary of all results is presented in Supporting Information 3.

The study on surface roughness was expanded at a smaller scale, by means of AFM analysis. Both R1 and R2's mapped surface images are presented in Figure 3.20.

R1 and R2's RMS (Root Mean Square) roughness values were measured from a single 20x20 μm area on each sample's surface. Unfortunately, both films reveal highly similar RMS roughness values, of 1.097 nm and 1.088 nm respectively, and results are regarded as inconclusive. Although these results are significantly lower, they are in the same order of magnitude as ones reported by *Lefebvre et al.*.[55].

Having shown outstanding optical and physical features, a small piece of R2's central region was broken off and later used in an assembled electro-optical cell, which was thoroughly studied.

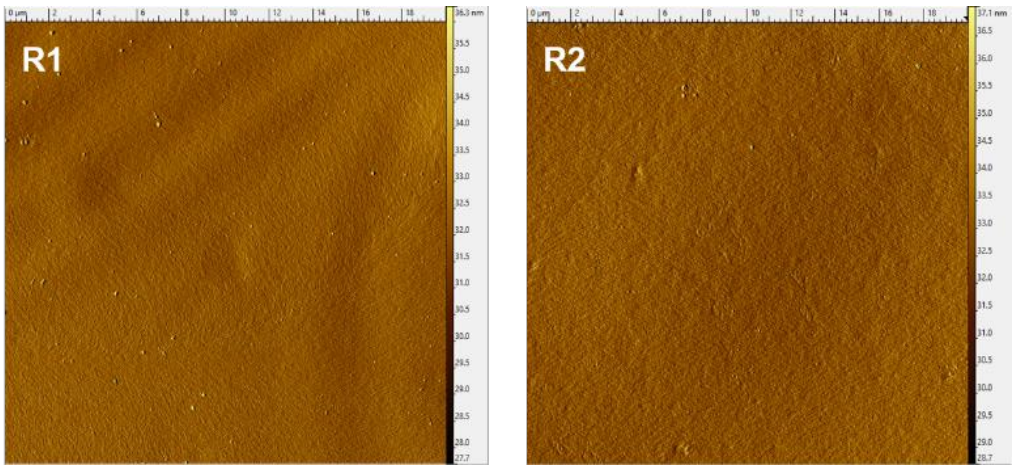

Figure 3.20 – AFM-captured images of a 20x20 μm surface area of R1 and R2, in amplitude retrace mode.

3.6 Electro-optical cell assembly using a freestanding CNC film

An electro-optical device was assembled where a portion from the R2 CNC film was inserted between two ITO-coated glasses and the cell was filled up with 5CB, as described previously in this thesis's Materials and Methods section. Photographical evidence, while observing the cell under left and right circularly polarised light, was captured and is shown in Figure 3.21 **a)** and **b)**.

The captured photographs now show no major change in the film's reflection, when comparing the LCP and RCP light channel images, as a reflection can be observed for both light channels. Observation of the POM images (Figure 3.21 **c)** and **d)**) reveals small changes in colour in certain domains of the

image (mainly shifting between green and red hues). RCP light is now mostly reflected, instead of being transmitted. In order to verify the CNC film's optical response while uninfluenced by the 5CB, temperature was raised up to 37 ºC, above the 5CB's nematic/isotropic phase transition threshold of 35 ºC. [56] As expected, RCP light reflection (Figure 3.21 **f**) is similar to that of previously presented experiments. At this point, the 5CB ceases to act as a half-wave retardation plate (see Figure 3.17 **d)**), confirming that the presence of 5CB effectively influences the CNC/5CB system optical behaviour, and that by temperature variation one can tune the 5CB birefringence.

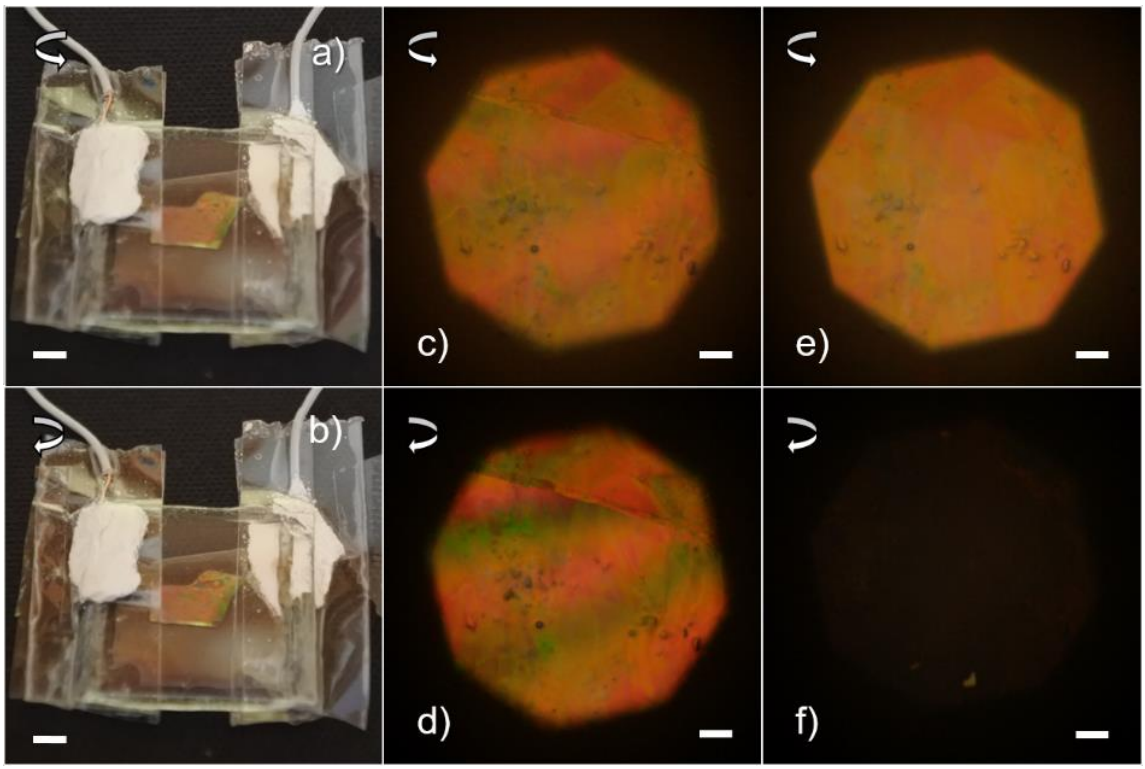

Figure 3.21 – **a), b)** LCP and RCP light channel photographs of the electro-optical cell, respectively; **c), d)** LCP and RCP light channel POM reflection images, respectively, while the 5CB is in the nematic phase; **e)**, **f)** LCP and RCP light channel POM reflection images, respectively, while the 5CB is in the isotropic phase. Scale bars for **a)**, **b)**: 2 mm. Scale bars for **c)** – **f)**.

A similar optical response has been reported by *Fernandes et al.* [11], who attributed its cause to the formation of a microscopic gap inside the film's cross-section, within which the 5CB was infiltrated. This way, the gap is filled with a nematic layer, functioning as a half-wave retardation plate between two CNC cholesteric layers.

The presence of a physical gap within the thin film R2 was investigated by observing a cross-section of an adjacent film section by SEM (Figure 3.22).

The cross-section image reveals a long transversal opening or microgap (604 ± 56 nm wide, averaged from 20 measurements) dividing the film into two separate cholesteric layers having different helicoidal pitches. It is noteworthy to mention that the microgap edges look slightly slanted, in relation to the observer's point of view, so the real microgap height may be marginally larger than the registered average value. From the obtained images, the average pitch lengths on either side of the gap were

unable to be measured and had to be deduced from the electro-optical cell's LCP and RCP channel reflectivity spectra (Figure 3.22 **b)**) by using the de Vries expression. The thickness values of the layers above and below the microgap were measured from a different SEM image, presented in Supporting Information 4. [10] Relevant data is shown in Table 2.

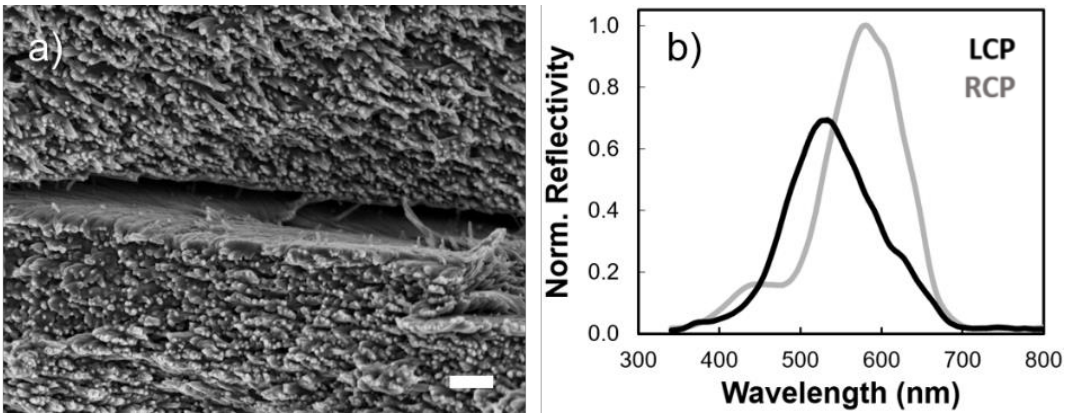

Figure 3.22 – **a)** SEM image of the microgap inside the CNC film. The gap extends far beyond the sides of the image, in reality, with varying gap widths along the way. **b)** LCP and RCP light reflectivity spectra, measured for wavelengths from 350 to 800 nm, of the centre of the electro-optical device. Spectra were normalized around the RCP light spectrum. Scale bar for **a)**: 500 nm.

Table 2 – Data acquired from Figure 3.22 **b)**. The wavelength peak is the wavelength value associated with each spectrum's maximum reflectivity value, the calculated pitch length is the extrapolated cholesteric pitch size from each respective wavelength peak (using the de Vries expression), and the spectral width is equivalent to FWHM value of each spectrum.

Polarised light channel	Wavelength peak (nm)	Calculated pitch length (nm)	Spectral width (nm)	Layer thickness (μm)
LCP	533	341	123	7.6
RCP	580	371	111	3.6

When comparing the exhibited data to the previously shown work of *Fernandes et al* [11], we can see their device reflects LCP and RCP light in similar magnitudes, while the one studied in this thesis demonstrates better reflectivity in the RCP light channel. Their obtained spectral peaks are very close to ours, both for the LCP light channel (reported wavelength of 520 nm vs. 533 nm) and the RCP light channel (reported wavelength of 600 nm vs. 580 nm). Lastly, spectral width values are also in good accordance with the ones presented by the authors.

Additional reflectance spectra were numerically simulated by means of a 4 × 4 Berreman matrix. [57] The simulations accounted for various physical values: the nematic 5CB birefringence, the pitch sizes and thickness values of the cholesteric domains above and below the film's microgap, and the microgap's height. Multiple simulations were carried out with these fixed values, varying only the microgap's height, from 500 to 1100 nm, in multiples of 100 nm. The simulated spectra, where a gap size equal to 800 nm was used, are shown in Figure 3.23.

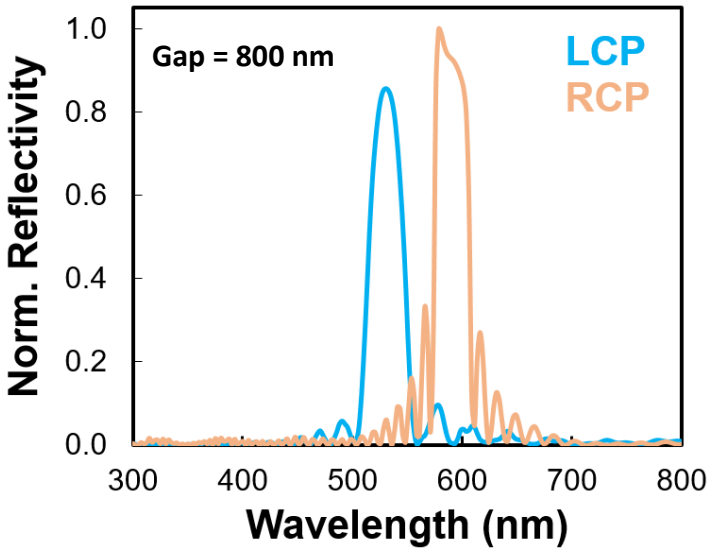

Figure 3.23 – Simulated reflectance spectra by means of a 4 × 4 Berreman matrix, for the LCP and RCP light channels, respectively.

Out of the obtained simulated spectra, for different gap sizes, the reflectance curves coinciding best with the experimental ones were the ones presented in Figure 3.23, suggesting that the CNC film's actual microgap height is, in fact, closer to 800 nm. Both spectra's peak wavelength values coincide similarly with the experimental reflectance curves (Figure 3.22 **b)**), however the simulated spectral width values are much thinner. This can be linked to the CNC film's heterogeneities, which are manifested as variations in pitch size and gap thickness values.

The electro-optical device's optical response to the application of an electric field was tested. POM images of the film's LCP and RCP light reflection were captured while an electric current was applied to each electrode and switched on and off (Figure 3.24 **a)** – **d)**). A real-time video recording of multiple on/off cycles is available in Supporting Information 5.

Prior to the images taken, the applied electric field was gradually intensified, up to 1.67 V/μm. With each increase, this led to a gradual improvement in the observed transmission, while in the on state. This value is in good accordance with reported results in literature (~ 1.6 V/μm) [11]. The effect of a larger amount of electric field was not tested, as not to risk damaging the embedded CNC film.

Optical response matches conclusions found in literature, as well. While in the off state, a large chromatic gradient is visible, more so in the RCP light channel image (Figure 3.24 **b)**). This can be attributed to an optical side effect due to the presence of 5CB in front of the film. In the on state, both channel images respond as expected: (Figure 3.24 **c)**) displays only the film's surface, with little to no visible nematic layer on top due to the electric field's influence; and (Figure 3.24 **d)**) exhibits a near-black reflection of the film, since all RCP light is transmitted. It should be noted that this outstanding response was observed to be similar throughout the extension of the CNC film.

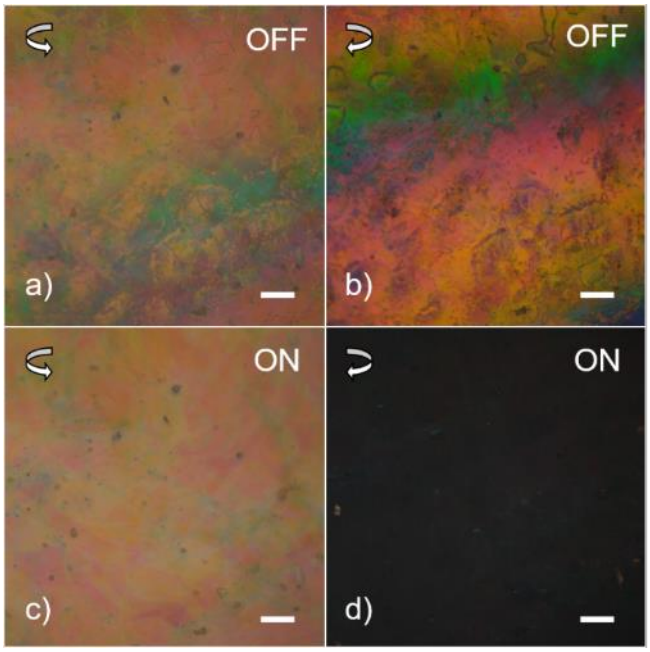

Figure 3.24 – **a), b)** POM reflection images of the LCP and RCP light channels of the electro-optical cell, respectively, while in the off state. The wide chromatic gradient in **b)** can be attributed to optical interference from the 5CB; **c), d)** POM images of the LCP and RCP light channels of the electro-optical cell, respectively, while in the on state. Scale bars:50 µm

4 Conclusion and future perspectives

This work's main objective was to optimize a CNC film's characteristic optical properties, by mainly improving its selective LCP light reflectivity and RCP light transmission, while aiming for the production of a structurally and chromatically uniform thin membrane. The number of variables explored, along with the variety of characterisation methods employed, allows us to assert that a significant amount of progress was made on the subject.

Cellulose nanocrystals were successfully obtained from the acid hydrolysis of microcrystalline cellulose. Starting from a particle size of ~50 mm it was possible to obtain cellulose nanocrystals with an average length of ~158 nm bearing a rice-like shape. The CNC's diffraction patterns show the presence of a cellulose type I structure, as observed in the original MCC fibres, however the CNC presents a higher crystalline index (I_C = 88.94 %) than MCC (I_C = 76.19 %). This result can be ascribed to the removal of the amorphous regions of the cellulose during the chemical treatment without disrupting its initial structure. Cellulose nanocrystals were suspended in water at different concentrations ranging from 2.8 % to 9.1 % (w/w). In all suspensions, a phase separation could be observed and the fraction of the anisotropic phase (bottom layer) increased as the CNC content in the suspension rose. This singular bright or birefringent layer, when observed between cross-polarisers, is attributed to the self-assembly of CNC into a cholesteric liquid crystalline phase.

The initial production of freestanding films, derived from the suspensions with varying CNC concentrations, allowed for various observations which fundamentally led this work's development process. Three films, from suspensions with CNC content of 2.8 %, 4.6% and 6.1% (w/w), were obtained displaying vibrant structural colours. A correlation was made between the increasing concentration values and the main reflected colour of each film's surface, suggesting that the reflected wavelength of the film's cholesteric structure decreases as CNC concentration rises in the precursor suspension. Despite the films' bright reflected colours, their spectral width is still large (ranging from 158 to ~ 200 nm), which can be attributed to a non-uniform arrangement of the cholesteric layers, both spatially and orientationally.

In an attempt to replicate the films' optical behaviour at a smaller scale, as to attenuate material and time resources, drop-cast CNC films were evaporated at different temperatures (3 ºC, 20 ºC and 60 ºC). A noticeable topographic difference was perceived with decreasing temperature of evaporation, showing a clear dissipation of the already reported "coffee stain" effect. It was suggested that this correlation is, in fact, linked to the rate of evaporation of each droplet, as a slower evaporation process should be tied to a weaker capillary flow within the droplet. This way, since a lesser amount of particles is transferred in the direction of the droplet's edges, a more uniform film can be obtained. If the films are observed at the same central point, one can see that a higher RCP light transmission is obtained from the droplet on the higher end of the evaporation temperature spectrum. Less RCP light is reflected at the centre of the film, where it is relatively thinner, so a link between the film thickness and its RCP light response may be possible.

Investigations using the drop-cast template resumed by exploring substrate hydrophobicity as a way to improve the film's structural homogeneity. An additional set of drop-cast films were evaporated at 3

ºC, with varying amounts of UV radiation applied to each substrate, resulting in thinner, more dispersed solid films. RCP light transmission in all samples was found to be vastly improved upon previous attempts, solidifying the hypothesis of optical response being tied to lesser thickness.

Studies progressed towards the production of even thinner freestanding films, while also exploring the possibility of an applied strong magnetic field during the evaporation process. Two very thin films were obtained, one was evaporated under the influence of a 7.05 T magnetic field (R2), the other was not (R1). The samples displayed surprisingly vibrant superficial colouring, along with a low degree of roughness (determined by AFM, and specular and diffuse reflectance spectroscopy). Microscopically, both presented a very good response in the RCP channel, demonstrating near-black tones. However, the magnetically influenced film stood out by showing a very consistent chromatic scheme, microscopically. This is further evidenced by its outstandingly low spectral width (105 nm), measured from its LCP light reflectivity spectrum.

A piece of R2 was implemented into an electro-optical device, by placing it between two ITO-coated glass substrates and impregnating it with a nematic liquid crystal (5CB). The device was optically tested, and results were in good agreement with literature [11], suggesting the existence of a microgap within the film's cholesteric layering. The presence of this physical gap was confirmed by SEM observation, and the electro-response was established by application of an electric field. The defined electric field value necessary for an optically responsive on state, 1.67 V/µm, was in good agreement with literature. In the RCP channel, at a microscopic level, the device exhibits red and green hues in the off state and shows near perfect transmission in the on state.

Although interesting results were obtained from the studies presented above, it can be seen that a full RCP transmission and low spectral width (in the order of tens of nanometers) of the structurally coloured CNC film is yet to be obtained. Along with the full control of the microgap's dimensions that arises from this cholesteric suspension of CNC. In order to be able to use these films in this type of electro-optical devices, further control of the aforementioned parameters is of paramount importance and one can envision some experiments that must be performed.

1) We can further delay the onset of the glassy state using the demonstrated way of slowing down a film's evaporation rate due to a low temperature, with a method recently proposed by Tran et al. [58] where the suspension's evaporation process is stalled by temporarily covering the system with a lid. Implementing both procedures should slow down the evaporation process as to enhance the uniformity of the film's helical orientation.

2) An attempt to mimic and control the CNC film's naturally assembled microgap may be explored by means of a stacking procedure inspired by the method presented by Hyunhee et al. [59] where the authors used a PVA layer to separate multiple thermotropic cholesteric liquid crystals into different pitch sizes

3) Production of new electro-optical devices, impregnated with different liquid crystalline substances, such as a cholesteric liquid crystal bearing a different handedness and a pitch reflecting light in the visible spectrum (hundreds of nanometers).

5 References

[1] P. Oswald and P. Pieranski, *Nematic and Cholesteric Liquid Crystals*. CRC Press, 2005.

[2] G. Pelzl and A. Hauser, “Birefringence and phase transitions in liquid crystals,” *Phase Transitions*, vol. 37, no. 1, pp. 33–62, 1991.

[3] S. Mohanty, “Liquid crystals — The ‘fourth’ phase of matter,” *Resonance*, vol. 8, no. November, pp. 52–70, 2003.

[4] A. F. Martins, “Os cristais líquidos,” *Independent*, vol. 7, p. 253, 1991.

[5] P. S. Pershan, “Lyotropic liquid crystals,” *Phys. Today*, vol. 35, no. 5, pp. 34–39, 1982.

[6] T. Niori, T. Sekine, J. Watanabe, T. Furukawa, and H. Takezoe, “Distinct ferroelectric smectic liquid crystals consisting of banana shaped achiral molecules,” *J. Mater. Chem.*, vol. 6, no. 7, p. 1231, 1996.

[7] H. J. Seo *et al.*, “Robust photonic microparticles comprising cholesteric liquid crystals for anti-forgery materials,” *J. Mater. Chem. C*, vol. 5, no. 30, pp. 7567–7573, 2017.

[8] V. Sharma, M. Crne, J. O. Park, and M. Srinivasarao, “Structural origin of circularly polarized iridescence in jeweled beetles,” *Science (80-.).*, vol. 325, no. 5939, pp. 449–451, 2009.

[9] A. P. C. Almeida, J. P. Canejo, S. N. Fernandes, C. Echeverria, P. L. Almeida, and M. H. Godinho, “Cellulose-Based Biomimetics and Their Applications,” *Adv. Mater.*, vol. 1703655, p. 1703655, Jan. 2018.

[10] A. G. Dumanli *et al.*, “Digital color in cellulose nanocrystal films,” *ACS Appl. Mater. Interfaces*, vol. 6, no. 15, pp. 12302–12306, 2014.

[11] S. N. Fernandes *et al.*, “Mind the Microgap in Iridescent Cellulose Nanocrystal Films,” *Adv. Mater.*, vol. 29, no. 2, p. 1603560, Jan. 2017.

[12] J. C. Payne and E. L. Thomas, “Towards an understanding of nanoparticle-chiral nematic liquid crystal co-assembly,” *Adv. Funct. Mater.*, vol. 17, no. 15, pp. 2717–2721, 2007.

[13] M. Mitov, “Cholesteric liquid crystals in living matter,” *Soft Matter*, vol. 13, no. 23, pp. 4176–4209, 2017.

[14] D. Klemm *et al.*, “Nanocelluloses: A new family of nature-based materials,” *Angew. Chemie - Int. Ed.*, vol. 50, no. 24, pp. 5438–5466, 2011.

[15] R. J. Moon, A. Martini, J. Nairn, J. Simonsen, and J. Youngblood, *Cellulose nanomaterials review: structure, properties and nanocomposites*, vol. 40, no. 7. 2011.

[16] R. M. Parker *et al.*, “The Self-Assembly of Cellulose Nanocrystals: Hierarchical Design of Visual Appearance,” *Adv. Mater.*, vol. 1704477, 2017.

[17] S. Beck-Candanedo, M. Roman, and D. G. Gray, “Effect of reaction conditions on the properties and behavior of wood cellulose nanocrystal suspensions,” *Biomacromolecules*, vol. 6, no. 2, pp. 1048–1054, 2005.

[18] J. H. Park *et al.*, “Macroscopic Control of Helix Orientation in Films Dried from Cholesteric Liquid-Crystalline Cellulose Nanocrystal Suspensions,” *ChemPhysChem*, vol. 15, no. 7, pp. 1477–1484, May 2014.

[19] X. Mu and D. G. Gray, “Droplets of cellulose nanocrystal suspensions on drying give iridescent 3-D ‘coffee-stain’ rings,” *Cellulose*, vol. 22, no. 2, pp. 1103–1107, 2015.

[20] A. Gençer, C. Schütz, and W. Thielemans, “Influence of the particle concentration and marangoni flow on the formation of cellulose nanocrystal films,” *Langmuir*, vol. 33, no. 1, pp. 228–234, 2017.

[21] G. Chu, R. Vilensky, G. Vasilyev, P. Martin, R. Zhang, and E. Zussman, “Structure Evolution and Drying Dynamics in Sliding Cholesteric Cellulose Nanocrystals,” *J. Phys. Chem. Lett.*, pp. 1845–1851, 2018.

[22] J. P. F. Lagerwall *et al.*, “Cellulose nanocrystal-based materials: from liquid crystal self-assembly and glass formation to multifunctional thin films,” *NPG Asia Mater.*, vol. 6, no. 1, pp. e80–e80, Jan. 2014.

[23] F. Bruno, R. Harisoa, J. Bruno, and H. Laurent, “Dynamically Controlled Iridescence of Cholesteric Cellulose Nanocrystal Suspensions Using Electric Fields,” *Adv. Mater.*, vol. 29, no. 11, p. 1606208, Jan. 2017.

[24] B. Frka-Petesic, G. Guidetti, G. Kamita, and S. Vignolini, “Controlling the Photonic Properties of Cholesteric Cellulose Nanocrystal Films with Magnets,” *Adv. Mater.*, vol. 29, no. 32, pp. 1–7, 2017.

[25] Y. Kun, M. Qijun, B. Vincent, and Z. Qi, “Flexible and Responsive Chiral Nematic Cellulose Nanocrystal/Poly(ethylene glycol) Composite Films with Uniform and Tunable Structural Color,” *Adv. Mater.*, vol. 29, no. 28, p. 1701323, Jul. 2017.

[26] J. Pan, W. Hamad, and S. K. Straus, “Parameters Affecting the Chiral Nematic Phase of Nanocrystalline Cellulose Films,” *Macromolecules*, vol. 43, no. 8, pp. 3851–3858, Apr. 2010.

[27] D. Gray, “Recent Advances in Chiral Nematic Structure and Iridescent Color of Cellulose Nanocrystal Films,” *Nanomaterials*, vol. 6, no. 11, p. 213, Nov. 2016.

[28] X. M. Dong and D. G. Gray, “Effect of Counterions on Ordered Phase Formation in Suspensions of Charged Rodlike Cellulose Crystallites,” *Langmuir*, vol. 13, no. 8, pp. 2404–2409, Apr. 1997.

[29] S. Beck, J. Bouchard, and R. Berry, “Controlling the Reflection Wavelength of Iridescent Solid Films of Nanocrystalline Cellulose,” *Biomacromolecules*, vol. 12, no. 1, pp. 167–172, Jan. 2011.

[30] T. Kato, “Self-assembly of phase-segregated liquid crystal structures,” *Science*, vol. 295, no. 5564. pp. 2414–2418, 2002.

[31] H. G. Craighead, J. Cheng, and S. Hackwood, “New display based on electrically induced index-matching in an inhomogeneous medium,” *Appl. Phys. Lett.*, vol. 40, no. 1, pp. 22–24, 1982.

[32] M. H. Godinhot, A. F. Martins, and J. L. Figueirinhas, “Novel pdlc type display based on cellulose derivatives,” *Liq. Cryst.*, vol. 20, no. 3, pp. 373–376, 1996.

[33] M. H. Godinho, A. F. Martins, and J. L. Figueirinhas, “Composite systems for display applications from cellulose elastomers and nematic liquid crystals,” *Opt. Mater. (Amst).*, vol. 9, no. 1–4, pp. 226–229, 1998.

[34] P. L. Almeida, M. H. Godinho, M. T. Cidade, and J. L. Figueirinhas, “Electro-Optical Properties of Cellulose Based PDLC Type Cells: Dependence on the Type of Diisocyanate Cross-Linking Agent Used,” *Mol. Cryst. Liq. Cryst. Sci. Technol. Sect. A. Mol. Cryst. Liq. Cryst.*, vol. 368, no. 1, pp. 121–128, 2001.

[35] Y. Geng, P. Brogueira, J. L. Figueirinhas, M. H. Godinho, and P. L. Almeida, “Light shutters from nanocrystalline cellulose rods in a nematic liquid crystal,” *Liq. Cryst.*, vol. 40, no. 6, pp. 769–773, 2013.

[36] P. J. Collings, “Liquid Crystals: Nature’s Delicate Phase of Matter,” *Am. J. Phys.*, vol. 60, no. 10, p. 958, 1992.

[37] M. J. Stephen and J. P. Straley, “Physics of liquid crystals,” *Rev. Mod. Phys.*, vol. 46, no. 4, pp. 617–704, 1974.

[38] J. F. Revol, H. Bradford, J. Giasson, R. H. Marchessault, and D. G. Gray, “Helicoidal self-ordering of cellulose microfibrils in aqueous suspension,” *Int. J. Biol. Macromol.*, vol. 14, no. 3, pp. 170–172, 1992.

[39] J. P. S. Morais, M. D. F. Rosa, M. D. S. M. De Souza Filho, L. D. Nascimento, D. M. Do Nascimento, and A. R. Cassales, “Extraction and characterization of nanocellulose structures from raw cotton linter,” *Carbohydr. Polym.*, vol. 91, no. 1, pp. 229–235, 2013.

[40] E. de Morais Teixeira, A. C. Corrêa, A. Manzoli, F. de Lima Leite, C. de Ribeiro Oliveira, and L. H. C. Mattoso, “Cellulose nanofibers from white and naturally colored cotton fibers,” *Cellulose*, vol. 17, no. 3, pp. 595–606, 2010.

[41] L. Segal, J. J. Creely, A. E. Martin, and C. M. Conrad, “An Empirical Method for Estimating the Degree of Crystallinity of Native Cellulose Using the X-Ray Diffractometer,” *Text. Res. J.*, vol. 29, no. 10, pp. 786–794, 1959.

[42] D. Gaspar *et al.*, “Nanocrystalline cellulose applied simultaneously as the gate dielectric and the

substrate in flexible field effect transistors," *Nanotechnology*, vol. 25, no. 9, p. 094008, Mar. 2014.

[43] W. Y. Hamad, *Cellulose Nanocrystals: Properties, Production and Applications*. 2017.

[44] R. H. Atalla and A. Isogai, *Recent Developments in Spectroscopic and Chemical Characterization of Cellulose Rajai*. 1998.

[45] N. F. Vasconcelos *et al.*, "Bacterial cellulose nanocrystals produced under different hydrolysis conditions: Properties and morphological features," *Carbohydr. Polym.*, vol. 155, pp. 425–431, 2017.

[46] C. Honorato-Rios, A. Kuhnhold, J. R. Bruckner, R. Dannert, T. Schilling, and J. P. F. Lagerwall, "Equilibrium Liquid Crystal Phase Diagrams and Detection of Kinetic Arrest in Cellulose Nanocrystal Suspensions," *Front. Mater.*, vol. 3, no. May, pp. 1–13, 2016.

[47] S. N. Fernandes *et al.*, "Structural color and iridescence in transparent sheared cellulosic films," *Macromol. Chem. Phys.*, vol. 214, no. 1, pp. 25–32, 2013.

[48] M. Ličen *et al.*, "Correlation between structural properties and iridescent colors of cellulose nanocrystalline films," *Cellulose*, vol. 23, no. 6, pp. 3601–3609, 2016.

[49] R. D. Deegan, O. Bakajin, T. F. Dupont, G. Huber, S. R. Nagel, and T. A. Witten, "Capillary flow as the causes of ring stains from dried liquid drops," *Nature, London*, vol. 389, pp. 827–829, 1997.

[50] M. Majumder *et al.*, "Overcoming the 'coffee-stain' effect by compositional marangoni-flow-assisted drop-drying," *J. Phys. Chem. B*, vol. 116, no. 22, pp. 6536–6542, 2012.

[51] R. L. DeRosa, P. A. Schader, and J. E. Shelby, "Hydrophilic nature of silicate glass surfaces as a function of exposure condition," *J. Non. Cryst. Solids*, vol. 331, no. 1–3, pp. 32–40, 2003.

[52] J. Drelich, E. Chibowski, D. D. Meng, and K. Terpilowski, "Hydrophilic and superhydrophilic surfaces and materials," *Soft Matter*, vol. 7, no. 21, p. 9804, 2011.

[53] B. Frka-Petesic, J. Sugiyama, S. Kimura, H. Chanzy, and G. Maret, "Negative Diamagnetic Anisotropy and Birefringence of Cellulose Nanocrystals," *Macromolecules*, vol. 48, no. 24, pp. 8844–8857, 2015.

[54] K. J. De France, K. G. Yager, T. Hoare, and E. D. Cranston, "Cooperative Ordering and Kinetics of Cellulose Nanocrystal Alignment in a Magnetic Field," *Langmuir*, vol. 32, no. 30, pp. 7564–7571, 2016.

[55] J. Lefebvre and D. G. Gray, "AFM of adsorbed polyelectrolytes on cellulose I surfaces spin-coated on silicon wafers," *Cellulose*, vol. 12, no. 2, pp. 127–134, 2005.

[56] G. a Bonvallet, "Differential Scanning Calorimetric Study of the Nematic Liquid Crystal 5CB," *Physics (College. Park. Md)*., pp. 1–4, 1999.

[57] D. W. Berreman, "Optics in Stratified and Anisotropic Media: 4x4-Matrix Formulation," *J. Opt. Soc. Am.*, vol. 62, no. 4, pp. 502–510, 1972.

[58] A. Tran, W. Y. Hamad, and M. J. MacLachlan, "Tactoid Annealing Improves Order in Self-Assembled Cellulose Nanocrystal Films with Chiral Nematic Structures," *Langmuir*, vol. 34, no. 2, pp. 646–652, Jan. 2018.

[59] C. Hyunhee *et al.*, "Broadband Cavity-Mode Lasing from Dye-Doped Nematic Liquid Crystals Sandwiched by Broadband Cholesteric Liquid Crystal Bragg Reflectors," *Adv. Mater.*, vol. 22, no. 24, pp. 2680–2684, Apr. 2010.

[60] LC-Science, "Fréedericksz transitions," 2018. [Online]. Available: http://www.lc-science.info/wordpress/wp-content/uploads/Freedericksz.jpg. [Accessed: 06-Apr-2018].

6 Supporting information

6.1 AFM measurements of length and width of individual CNC particles

Parameter	Measurement	a	b	c	d	e	f	g	h	i	j
length (nm)	1	158.26	163.24	95.01	164.39	123.59	153.43	217.01	198.57	150.45	135.25
	2	207.93	228.22	121.31	140.21	127.39	184.03	120.33	92.46	146.83	157.68
	3	157.60	175.93	156.19	217.27	138.11	162.20	125.79	201.81	166.09	83.12
	4	213.19	120.25	172.13	220.80	265.41	197.45	131.12	179.06	198.51	156.93
	5	125.22	187.26	128.79	181.10	164.19	164.25	120.97	178.81	139.14	168.62
	6	138.69	196.36	152.19	112.26	185.35	162.63	278.23	139.92	165.94	163.70
	7	158.89	280.47	116.62	149.24	130.94	143.50	237.72	165.35	149.45	134.06
	8	112.52	99.15	141.71	163.88	136.81	169.40	180.19	150.81	109.88	97.85
	9	116.31	132.82	156.32	180.97	158.71	151.96	209.83	136.85	133.17	162.33
	10	104.21	90.69	126.07	202.05	174.96	143.82	177.86	200.45	126.36	132.19
	11	113.03	148.26	120.62	138.96	170.98	130.23	191.59	201.15	178.53	176.78
	12	243.66	134.25	171.21	149.71	161.58	144.51	121.40	101.69	162.04	176.78
	13	180.93	195.09	118.28	148.65	102.20	148.46	136.97	147.88	179.68	141.87
	14	171.98	158.34	190.17	157.47	163.53	272.80	148.85	117.90	141.00	134.81
	15	199.01	141.53	158.25	136.57	141.23	138.06	144.16	147.12	131.98	214.94
width (nm)	1	28.64	31.47	24.83	41.70	40.51	57.32	41.29	28.04	45.55	56.31
	2	25.08	30.65	37.17	29.52	45.26	37.17	43.49	41.70	47.95	44.12
	3	31.40	21.03	23.05	49.87	30.99	42.05	57.28	49.56	56.73	48.88
	4	16.62	30.92	20.62	35.11	39.17	47.46	53.61	35.05	36.53	48.09
	5	27.12	21.23	16.62	37.84	30.93	38.01	46.33	42.05	47.60	36.01
	6	18.56	29.16	35.11	32.20	50.92	43.35	39.17	45.22	55.71	40.03
	7	32.60	31.54	23.51	32.27	36.06	42.50	34.31	44.60	40.03	36.71
	8	35.23	30.99	28.04	34.99	35.05	50.54	32.60	44.41	38.90	39.66
	9	19.56	42.30	27.74	42.30	29.52	48.09	47.01	39.66	24.83	47.01
	10	23.51	28.94	28.04	37.17	29.73	29.16	37.17	53.76	43.35	31.47
	11	27.66	30.99	30.44	45.21	32.20	40.92	37.11	45.26	22.30	39.65
	12	15.70	35.05	22.68	45.78	36.71	43.34	46.10	53.76	30.65	35.11
	13	26.80	32.60	24.13	53.96	37.11	35.29	33.05	49.91	35.23	37.17
	14	34.56	28.04	21.52	33.24	35.05	40.61	37.62	52.80	25.50	32.60
	15	23.32	20.62	54.89	21.52	41.29	36.47	39.23	52.48	37.34	32.00

6.2 **Evaporation rate depending on temperature**

For each graph, the evaporation rate was calculated by averaging the slopes extrapolated from linear regressions for each sample. The linear regressions for each sample were fit using all points from its starting evaporation time to the first point where total mass reached 10% of the initial mass.

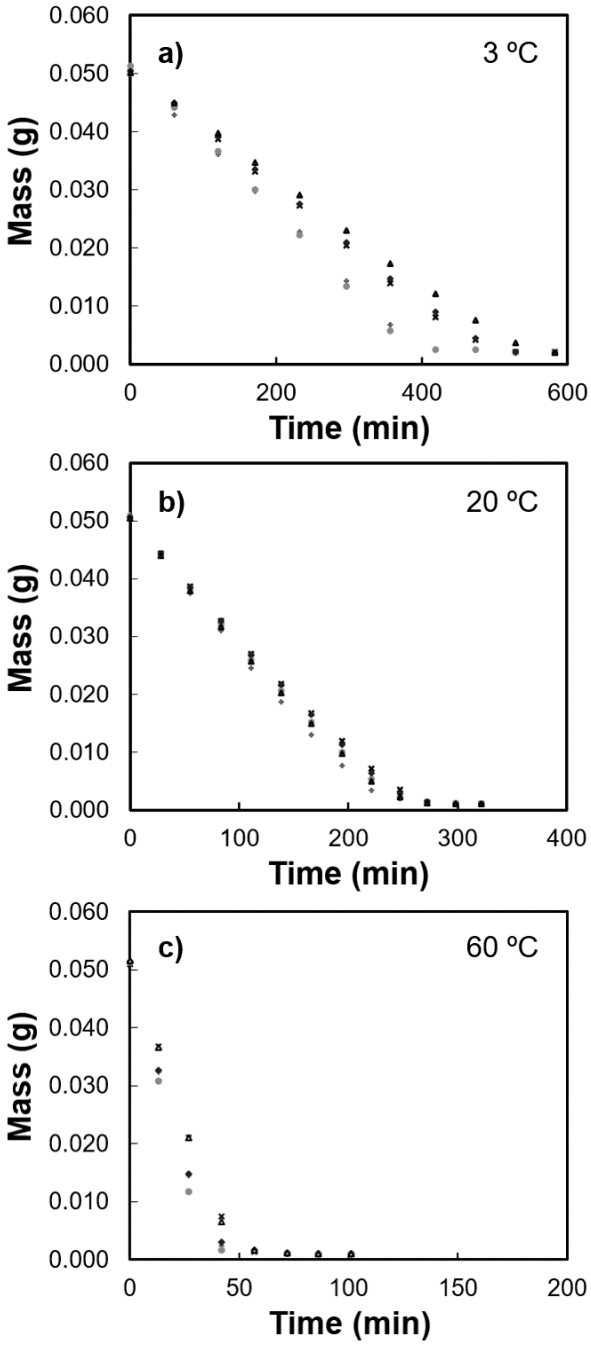

Figure 6.1 – a). b), c) Evaporation rate graphs for samples evaporated at 3 ºC, 20 ºC, and 60 ºC, respectively. Each different symbol represents a different arbitrary sample, out of a total of 5 for each tested temperature.

6.3 Specular and diffuse reflectance spectra for remaining films

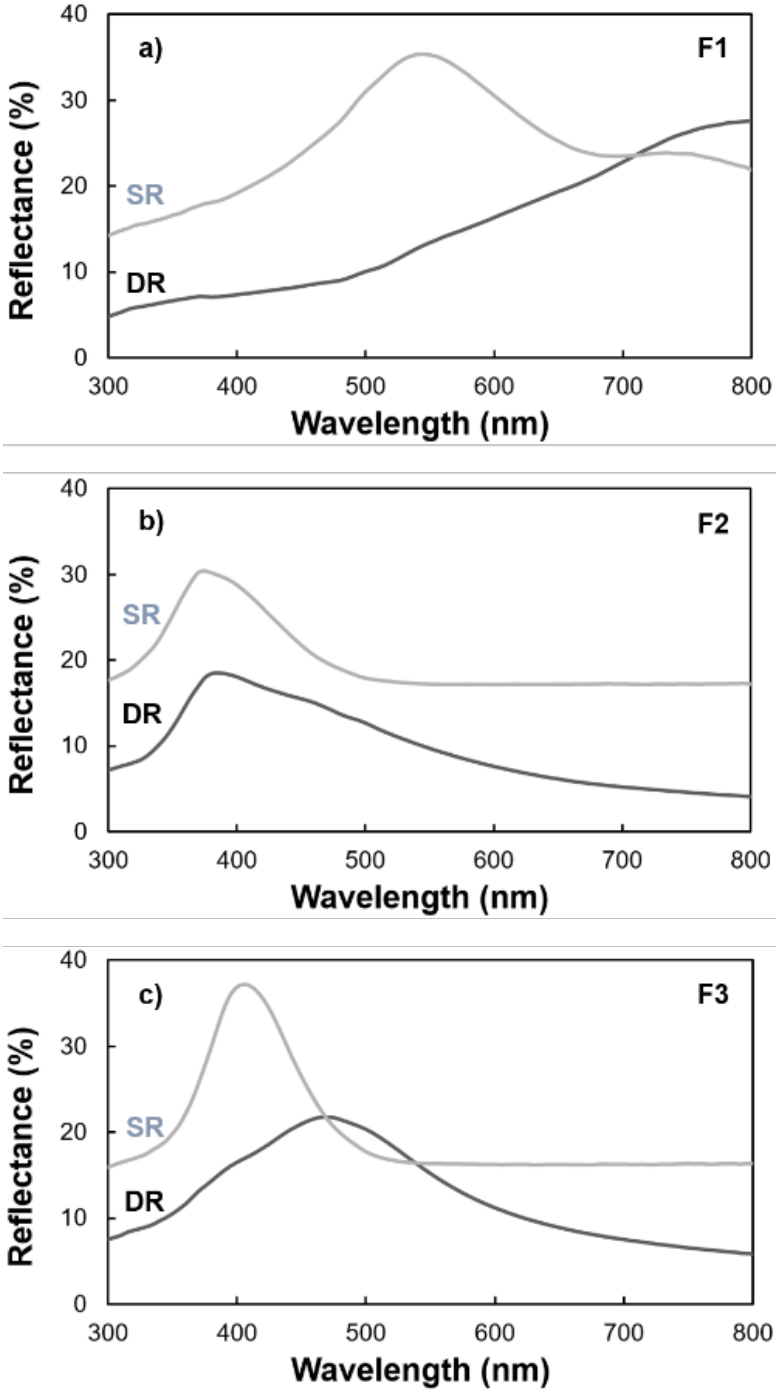

Figure 6.2 – **a), b), c)** Specular and diffuse reflectivity spectra for F1, F2, and F3, respectively. It is clear that, when compared to samples R1 and R2, these films showcase a much higher diffuse reflectivity relative to their specular reflectivity. SR stands for specular reflectivity, while DR stands for diffuse reflectivity.

6.4 SEM images used in the measuring of additional physical features

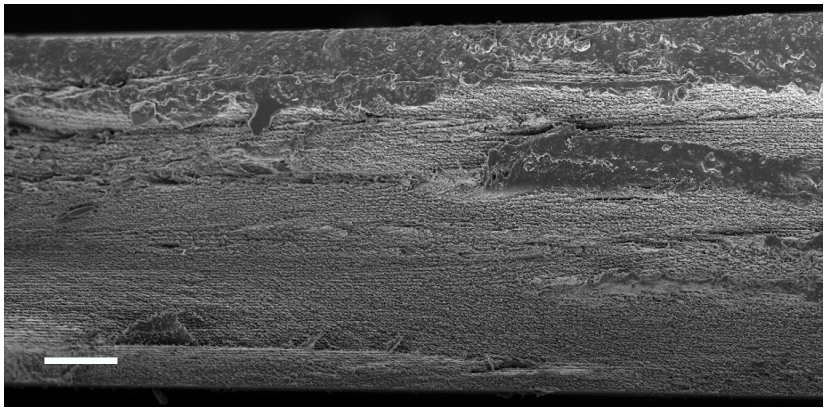

Figure 6.3 – SEM image of the full extension of the drop-cast film's cross-section. Scale bar: 5 μm.

The upper and lower cholesteric layer measurements were taken from Figure 6.4, below. A total of 20 measurements for each layer was registered.

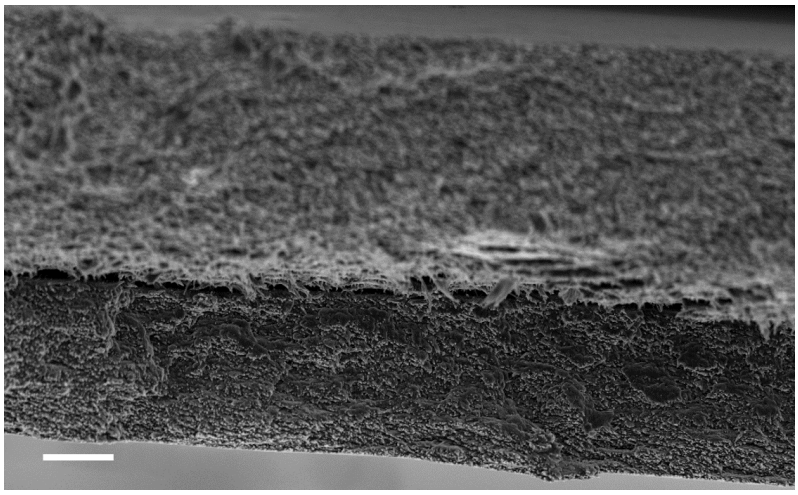

Figure 6.4 – SEM image of the full extension of the freestanding CNC film's cross-section. One can identify the microgap as the small opening near the centre. The upper and lower cholesteric layers are above and below it, respectively. Scale bar: 2 μm.

6.5 Videos displaying on and off cycles for the electro-optical cell

Two separate videos of the electro-optical cell switching between the ON and OFF states. The applied electric field value in the ON state was 1.67 V/μm. Each video corresponds to the LCP and RCP light channel, respectively, and are hosted online at:

Reversible electric field effect, LCP channel: **https://youtu.be/dN5OvhtDc7g** ;

Reversible electric field effect, RCP channel: **https://youtu.be/DFYdbLIRVNY** .

ROYAL SOCIETY OF CHEMISTRY LICENSE
TERMS AND CONDITIONS

Jun 22, 2018

This Agreement between Faculdade de Ciências e Tecnologia -- Diogo Saraiva ("You") and Royal Society of Chemistry ("Royal Society of Chemistry") consists of your license details and the terms and conditions provided by Royal Society of Chemistry and Copyright Clearance Center.

License Number	4372440585759
License date	Jun 19, 2018
Licensed Content Publisher	Royal Society of Chemistry
Licensed Content Publication	Chemical Society Reviews
Licensed Content Title	Cellulose nanomaterials review: structure, properties and nanocomposites
Licensed Content Author	Robert J. Moon,Ashlie Martini,John Nairn,John Simonsen,Jeff Youngblood
Licensed Content Date	May 12, 2011
Licensed Content Volume	40
Licensed Content Issue	7
Type of Use	Thesis/Dissertation
Requestor type	academic/educational
Portion	figures/tables/images
Number of figures/tables/images	1
Format	electronic
Distribution quantity	10
Will you be translating?	no
Order reference number	
Title of the thesis/dissertation	Electro-optical devices based on cellulose nanocrystals
Expected completion date	Jun 2018
Estimated size	55
Requestor Location	Faculdade de Ciências e Tecnologia Rua 25 de Novembro de 1975, Nr 2, 10A Miraflores Algés, Lisboa 1495-156 Portugal Attn: Diogo Saraiva
Billing Type	Invoice
Billing Address	Faculdade de Ciências e Tecnologia Rua 25 de Novembro de 1975, Nr 2, 10A Miraflores Algés, Portugal 1495-156

Attn: Diogo Saraiva

Total 0.00 EUR

Terms and Conditions

This License Agreement is between {Requestor Name} (“You”) and The Royal Society of Chemistry (“RSC”) provided by the Copyright Clearance Center (“CCC”). The license consists of your order details, the terms and conditions provided by the Royal Society of Chemistry, and the payment terms and conditions.

RSC / TERMS AND CONDITIONS

INTRODUCTION
The publisher for this copyrighted material is The Royal Society of Chemistry. By clicking “accept” in connection with completing this licensing transaction, you agree that the following terms and conditions apply to this transaction (along with the Billing and Payment terms and conditions established by CCC, at the time that you opened your RightsLink account and that are available at any time at .

LICENSE GRANTED
The RSC hereby grants you a non-exclusive license to use the aforementioned material anywhere in the world subject to the terms and conditions indicated herein. Reproduction of the material is confined to the purpose and/or media for which permission is hereby given.

RESERVATION OF RIGHTS
The RSC reserves all rights not specifically granted in the combination of (i) the license details provided by your and accepted in the course of this licensing transaction; (ii) these terms and conditions; and (iii) CCC’s Billing and Payment terms and conditions.

REVOCATION
The RSC reserves the right to revoke this license for any reason, including, but not limited to, advertising and promotional uses of RSC content, third party usage, and incorrect source figure attribution.

THIRD-PARTY MATERIAL DISCLAIMER
If part of the material to be used (for example, a figure) has appeared in the RSC publication with credit to another source, permission must also be sought from that source. If the other source is another RSC publication these details should be included in your RightsLink request. If the other source is a third party, permission must be obtained from the third party. The RSC disclaims any responsibility for the reproduction you make of items owned by a third party.

PAYMENT OF FEE
If the permission fee for the requested material is waived in this instance, please be advised that any future requests for the reproduction of RSC materials may attract a fee.

ACKNOWLEDGEMENT
The reproduction of the licensed material must be accompanied by the following acknowledgement:

Reproduced (“Adapted” or “in part”) from {Reference Citation} (or Ref XX) with permission of The Royal Society of Chemistry.

If the licensed material is being reproduced from New Journal of Chemistry (NJC), Photochemical & Photobiological Sciences (PPS) or Physical Chemistry Chemical Physics (PCCP) you must include one of the following acknowledgements:

For figures originally published in NJC:

Reproduced (“Adapted” or “in part”) from {Reference Citation} (or Ref XX) with permission of The Royal Society of Chemistry (RSC) on behalf of the European Society for Photobiology, the European Photochemistry Association and the RSC.

For figures originally published in PPS:

Reproduced (“Adapted” or “in part”) from {Reference Citation} (or Ref XX) with permission of The Royal Society of Chemistry (RSC) on behalf of the Centre National de la Recherche Scientifique (CNRS) and the RSC.

For figures originally published in PCCP:

Reproduced (“Adapted” or “in part”) from {Reference Citation} (or Ref XX) with permission of the PCCP Owner Societies.

HYPERTEXT LINKS
With any material which is being reproduced in electronic form, you must include a hypertext link to the original RSC article on the RSC’s website. The recommended form for the hyperlink is http://dx.doi.org/10.1039/DOI suffix, for example in the link http://dx.doi.org/10.1039/b110420a the DOI suffix is ‘b110420a’. To find the relevant DOI suffix for the RSC article in question, go to the Journals section of the website and locate the article in the list of papers for the volume and issue of your specific journal. You will find the DOI suffix quoted there.

LICENSE CONTINGENT ON PAYMENT
While you may exercise the rights licensed immediately upon issuance of the license at the end of the licensing process for the transaction, provided that you have disclosed complete and accurate details of your proposed use, no license is finally effective unless and until full payment is received from you (by CCC) as provided in CCC's Billing and Payment terms and conditions. If full payment is not received on a timely basis, then any license preliminarily granted shall be deemed automatically revoked and shall be void as if never granted. Further, in the event that you breach any of these terms and conditions or any of CCC's Billing and Payment terms and conditions, the license is automatically revoked and shall be void as if never granted. Use of materials as described in a revoked license, as well as any use of the materials beyond the scope of an unrevoked license, may constitute copyright infringement and the RSC reserves the right to take any and all action to protect its copyright in the materials.

WARRANTIES
The RSC makes no representations or warranties with respect to the licensed material.

INDEMNITY
You hereby indemnify and agree to hold harmless the RSC and the CCC, and their respective officers, directors, trustees, employees and agents, from and against any and all claims arising out of your use of the licensed material other than as specifically authorized pursuant to this licence.

NO TRANSFER OF LICENSE
This license is personal to you or your publisher and may not be sublicensed, assigned, or transferred by you to any other person without the RSC's written permission.

NO AMENDMENT EXCEPT IN WRITING
This license may not be amended except in a writing signed by both parties (or, in the case of “Other Conditions, v1.2”, by CCC on the RSC's behalf).

OBJECTION TO CONTRARY TERMS
You hereby acknowledge and agree that these terms and conditions, together with CCC's Billing and Payment terms and conditions (which are incorporated herein), comprise the entire agreement between you and the RSC (and CCC) concerning this licensing transaction, to the exclusion of all other terms and conditions, written or verbal, express or implied (including any terms contained in any purchase order, acknowledgment, check endorsement or other writing prepared by you). In the event of any conflict between your obligations established by these terms and conditions and those established by CCC's Billing and Payment terms and conditions, these terms and conditions shall control.

JURISDICTION
This license transaction shall be governed by and construed in accordance with the laws of the District of Columbia. You hereby agree to submit to the jurisdiction of the courts located in the District of Columbia for purposes of resolving any disputes that may arise in connection with this licensing transaction.

LIMITED LICENSE
The following terms and conditions apply to specific license types:

Translation
This permission is granted for non-exclusive world English rights only unless your license was granted for translation rights. If you licensed translation rights you may only translate this content into the languages you requested. A professional translator must perform all translations and reproduce the content word for word preserving the integrity of the article.

Intranet
If the licensed material is being posted on an Intranet, the Intranet is to be password-protected and made available only to bona fide students or employees only. All content posted to the Intranet must maintain the copyright information line on the bottom of each image. You must also fully reference the material and include a hypertext link as specified above.

Copies of Whole Articles
All copies of whole articles must maintain, if available, the copyright information line on the bottom of each page.

Other Conditions
v1.2

Gratis licenses (referencing $0 in the Total field) are free. Please retain this printable license for your reference. No payment is required.

If you would like to pay for this license now, please remit this license along with yourpayment made payable to "COPYRIGHT CLEARANCE CENTER" otherwise you will be invoiced within 48 hours of the license date. Payment should be in the form of a check or money order referencing your account number and this invoice number {Invoice Number}.

Once you receive your invoice for this order, you may pay your invoice by credit card.

Please follow instructions provided at that time.

Make Payment To:
Copyright Clearance Center
29118 Network Place
Chicago, IL 60673-1291

For suggestions or comments regarding this order, contact Rightslink Customer Support: customercare@copyright.com or +1-855-239-3415 (toll free in the US) or +1-978-646-2777.

Questions? customercare@copyright.com or +1-855-239-3415 (toll free in the US) or +1-978-646-2777.

JOHN WILEY AND SONS LICENSE
TERMS AND CONDITIONS

Jun 22, 2018

This Agreement between Faculdade de Ciências e Tecnologia -- Diogo Saraiva ("You") and John Wiley and Sons ("John Wiley and Sons") consists of your license details and the terms and conditions provided by John Wiley and Sons and Copyright Clearance Center.

License Number	4373910327277
License date	Jun 21, 2018
Licensed Content Publisher	John Wiley and Sons
Licensed Content Publication	Advanced Materials
Licensed Content Title	Mind the Microgap in Iridescent Cellulose Nanocrystal Films
Licensed Content Author	Susete N. Fernandes, Pedro L. Almeida, Nuno Monge, et al
Licensed Content Date	Nov 9, 2016
Licensed Content Volume	29
Licensed Content Issue	2
Licensed Content Pages	7
Type of use	Dissertation/Thesis
Requestor type	University/Academic
Format	Electronic
Portion	Figure/table
Number of figures/tables	1
Original Wiley figure/table number(s)	Figure 2
Will you be translating?	No
Title of your thesis / dissertation	Electro-optical devices based on cellulose nanocrystals
Expected completion date	Jul 2018
Expected size (number of pages)	1
Requestor Location	Faculdade de Ciências e Tecnologia Rua 25 de Novembro de 1975, Nr 2, 10A Miraflores Algés, Lisboa 1495-156 Portugal Attn: Diogo Saraiva
Publisher Tax ID	EU826007151
Total	0.00 EUR
Terms and Conditions	

TERMS AND CONDITIONS

This copyrighted material is owned by or exclusively licensed to John Wiley & Sons, Inc. or one of its group companies (each a"Wiley Company") or handled on behalf of a society with which a Wiley Company has exclusive publishing rights in relation to a particular work

(collectively "WILEY"). By clicking "accept" in connection with completing this licensing transaction, you agree that the following terms and conditions apply to this transaction (along with the billing and payment terms and conditions established by the Copyright Clearance Center Inc., ("CCC's Billing and Payment terms and conditions"), at the time that you opened your RightsLink account (these are available at any time at http://myaccount.copyright.com).

Terms and Conditions

- The materials you have requested permission to reproduce or reuse (the "Wiley Materials") are protected by copyright.

- You are hereby granted a personal, non-exclusive, non-sub licensable (on a stand-alone basis), non-transferable, worldwide, limited license to reproduce the Wiley Materials for the purpose specified in the licensing process. This license, **and any CONTENT (PDF or image file) purchased as part of your order,** is for a one-time use only and limited to any maximum distribution number specified in the license. The first instance of republication or reuse granted by this license must be completed within two years of the date of the grant of this license (although copies prepared before the end date may be distributed thereafter). The Wiley Materials shall not be used in any other manner or for any other purpose, beyond what is granted in the license. Permission is granted subject to an appropriate acknowledgement given to the author, title of the material/book/journal and the publisher. You shall also duplicate the copyright notice that appears in the Wiley publication in your use of the Wiley Material. Permission is also granted on the understanding that nowhere in the text is a previously published source acknowledged for all or part of this Wiley Material. Any third party content is expressly excluded from this permission.

- With respect to the Wiley Materials, all rights are reserved. Except as expressly granted by the terms of the license, no part of the Wiley Materials may be copied, modified, adapted (except for minor reformatting required by the new Publication), translated, reproduced, transferred or distributed, in any form or by any means, and no derivative works may be made based on the Wiley Materials without the prior permission of the respective copyright owner.**For STM Signatory Publishers clearing permission under the terms of the STM Permissions Guidelines only, the terms of the license are extended to include subsequent editions and for editions in other languages, provided such editions are for the work as a whole in situ and does not involve the separate exploitation of the permitted figures or extracts,** You may not alter, remove or suppress in any manner any copyright, trademark or other notices displayed by the Wiley Materials. You may not license, rent, sell, loan, lease, pledge, offer as security, transfer or assign the Wiley Materials on a stand-alone basis, or any of the rights granted to you hereunder to any other person.

- The Wiley Materials and all of the intellectual property rights therein shall at all times remain the exclusive property of John Wiley & Sons Inc, the Wiley Companies, or their respective licensors, and your interest therein is only that of having possession of and the right to reproduce the Wiley Materials pursuant to Section 2 herein during the continuance of this Agreement. You agree that you own no right, title or interest in or to the Wiley Materials or any of the intellectual property rights therein. You shall have no rights hereunder other than the license as provided for above in Section 2. No right, license or interest to any trademark, trade name, service mark or other branding ("Marks") of WILEY or its licensors is granted hereunder, and you agree that you shall not assert any such right, license or interest with respect thereto

- NEITHER WILEY NOR ITS LICENSORS MAKES ANY WARRANTY OR REPRESENTATION OF ANY KIND TO YOU OR ANY THIRD PARTY, EXPRESS, IMPLIED OR STATUTORY, WITH RESPECT TO THE MATERIALS OR THE ACCURACY OF ANY INFORMATION CONTAINED IN THE MATERIALS, INCLUDING, WITHOUT LIMITATION, ANY IMPLIED WARRANTY OF MERCHANTABILITY, ACCURACY, SATISFACTORY QUALITY, FITNESS FOR A PARTICULAR PURPOSE, USABILITY, INTEGRATION OR NON-INFRINGEMENT AND ALL SUCH WARRANTIES ARE HEREBY EXCLUDED BY WILEY AND ITS LICENSORS AND WAIVED BY YOU.

- WILEY shall have the right to terminate this Agreement immediately upon breach of this Agreement by you.

- You shall indemnify, defend and hold harmless WILEY, its Licensors and their respective directors, officers, agents and employees, from and against any actual or threatened claims, demands, causes of action or proceedings arising from any breach of this Agreement by you.

- IN NO EVENT SHALL WILEY OR ITS LICENSORS BE LIABLE TO YOU OR ANY OTHER PARTY OR ANY OTHER PERSON OR ENTITY FOR ANY SPECIAL, CONSEQUENTIAL, INCIDENTAL, INDIRECT, EXEMPLARY OR PUNITIVE DAMAGES, HOWEVER CAUSED, ARISING OUT OF OR IN CONNECTION WITH THE DOWNLOADING, PROVISIONING, VIEWING OR USE OF THE MATERIALS REGARDLESS OF THE FORM OF ACTION, WHETHER FOR BREACH OF CONTRACT, BREACH OF WARRANTY, TORT, NEGLIGENCE, INFRINGEMENT OR OTHERWISE (INCLUDING, WITHOUT LIMITATION, DAMAGES BASED ON LOSS OF PROFITS, DATA, FILES, USE, BUSINESS OPPORTUNITY OR CLAIMS OF THIRD PARTIES), AND WHETHER OR NOT THE PARTY HAS BEEN ADVISED OF THE POSSIBILITY OF SUCH DAMAGES. THIS LIMITATION SHALL APPLY NOTWITHSTANDING ANY FAILURE OF ESSENTIAL PURPOSE OF ANY LIMITED REMEDY PROVIDED HEREIN.

- Should any provision of this Agreement be held by a court of competent jurisdiction to be illegal, invalid, or unenforceable, that provision shall be deemed amended to achieve as nearly as possible the same economic effect as the original provision, and the legality, validity and enforceability of the remaining provisions of this Agreement shall not be affected or impaired thereby.

- The failure of either party to enforce any term or condition of this Agreement shall not constitute a waiver of either party's right to enforce each and every term and condition of this Agreement. No breach under this agreement shall be deemed waived or excused by either party unless such waiver or consent is in writing signed by the party granting such waiver or consent. The waiver by or consent of a party to a breach of any provision of this Agreement shall not operate or be construed as a waiver of or consent to any other or subsequent breach by such other party.

- This Agreement may not be assigned (including by operation of law or otherwise) by you without WILEY's prior written consent.

- Any fee required for this permission shall be non-refundable after thirty (30) days from receipt by the CCC.

- These terms and conditions together with CCC's Billing and Payment terms and

conditions (which are incorporated herein) form the entire agreement between you and WILEY concerning this licensing transaction and (in the absence of fraud) supersedes all prior agreements and representations of the parties, oral or written. This Agreement may not be amended except in writing signed by both parties. This Agreement shall be binding upon and inure to the benefit of the parties' successors, legal representatives, and authorized assigns.

- In the event of any conflict between your obligations established by these terms and conditions and those established by CCC's Billing and Payment terms and conditions, these terms and conditions shall prevail.

- WILEY expressly reserves all rights not specifically granted in the combination of (i) the license details provided by you and accepted in the course of this licensing transaction, (ii) these terms and conditions and (iii) CCC's Billing and Payment terms and conditions.

- This Agreement will be void if the Type of Use, Format, Circulation, or Requestor Type was misrepresented during the licensing process.

- This Agreement shall be governed by and construed in accordance with the laws of the State of New York, USA, without regards to such state's conflict of law rules. Any legal action, suit or proceeding arising out of or relating to these Terms and Conditions or the breach thereof shall be instituted in a court of competent jurisdiction in New York County in the State of New York in the United States of America and each party hereby consents and submits to the personal jurisdiction of such court, waives any objection to venue in such court and consents to service of process by registered or certified mail, return receipt requested, at the last known address of such party.

WILEY OPEN ACCESS TERMS AND CONDITIONS

Wiley Publishes Open Access Articles in fully Open Access Journals and in Subscription journals offering Online Open. Although most of the fully Open Access journals publish open access articles under the terms of the Creative Commons Attribution (CC BY) License only, the subscription journals and a few of the Open Access Journals offer a choice of Creative Commons Licenses. The license type is clearly identified on the article.

The Creative Commons Attribution License

The Creative Commons Attribution License (CC-BY) allows users to copy, distribute and transmit an article, adapt the article and make commercial use of the article. The CC-BY license permits commercial and non-

Creative Commons Attribution Non-Commercial License

The Creative Commons Attribution Non-Commercial (CC-BY-NC)License permits use, distribution and reproduction in any medium, provided the original work is properly cited and is not used for commercial purposes.(see below)

Creative Commons Attribution-Non-Commercial-NoDerivs License

The Creative Commons Attribution Non-Commercial-NoDerivs License (CC-BY-NC-ND) permits use, distribution and reproduction in any medium, provided the original work is properly cited, is not used for commercial purposes and no modifications or adaptations are

made. (see below)

Use by commercial "for-profit" organizations

Use of Wiley Open Access articles for commercial, promotional, or marketing purposes requires further explicit permission from Wiley and will be subject to a fee.

Further details can be found on Wiley Online Library
http://olabout.wiley.com/WileyCDA/Section/id-410895.html

Other Terms and Conditions:

v1.10 Last updated September 2015

Questions? customercare@copyright.com or +1-855-239-3415 (toll free in the US) or +1-978-646-2777.

SPRINGER NATURE LICENSE
TERMS AND CONDITIONS

Jun 22, 2018

This Agreement between Faculdade de Ciências e Tecnologia -- Diogo Saraiva ("You") and Springer Nature ("Springer Nature") consists of your license details and the terms and conditions provided by Springer Nature and Copyright Clearance Center.

License Number	4373360164497
License date	Jun 20, 2018
Licensed Content Publisher	Springer Nature
Licensed Content Publication	Nature
Licensed Content Title	In Retrospect: Twenty years of drying droplets
Licensed Content Author	Ronald G. Larson
Licensed Content Date	Oct 25, 2017
Licensed Content Volume	550
Licensed Content Issue	7677
Type of Use	Thesis/Dissertation
Requestor type	academic/university or research institute
Format	electronic
Portion	figures/tables/illustrations
Number of figures/tables/illustrations	1
High-res required	no
Will you be translating?	no
Circulation/distribution	<501
Author of this Springer Nature content	no
Title	Electro-optical devices based on cellulose nanocrystals
Instructor name	Susete Fernandes
Institution name	Faculdade de Ciências e Tecnologia
Expected presentation date	Jul 2018
Portions	Figure 1
Requestor Location	Faculdade de Ciências e Tecnologia Rua 25 de Novembro de 1975, Nr 2, 10A Miraflores Algés, Lisboa 1495-156 Portugal Attn: Diogo Saraiva
Billing Type	Invoice
Billing Address	Faculdade de Ciências e Tecnologia Rua 25 de Novembro de 1975, Nr 2, 10A Miraflores Algés, Portugal 1495-156

Attn: Diogo Saraiva

Total 0.00 EUR

Terms and Conditions

Springer Nature Terms and Conditions for RightsLink Permissions

Springer Customer Service Centre GmbH (the Licensor) hereby grants you a non-exclusive, world-wide licence to reproduce the material and for the purpose and requirements specified in the attached copy of your order form, and for no other use, subject to the conditions below:

1. The Licensor warrants that it has, to the best of its knowledge, the rights to license reuse of this material. However, you should ensure that the material you are requesting is original to the Licensor and does not carry the copyright of another entity (as credited in the published version).

   If the credit line on any part of the material you have requested indicates that it was reprinted or adapted with permission from another source, then you should also seek permission from that source to reuse the material.

2. Where **print only** permission has been granted for a fee, separate permission must be obtained for any additional electronic re-use.

3. Permission granted **free of charge** for material in print is also usually granted for any electronic version of that work, provided that the material is incidental to your work as a whole and that the electronic version is essentially equivalent to, or substitutes for, the print version.

4. A licence for 'post on a website' is valid for 12 months from the licence date. This licence does not cover use of full text articles on websites.

5. Where '**reuse in a dissertation/thesis**' has been selected the following terms apply: Print rights for up to 100 copies, electronic rights for use only on a personal website or institutional repository as defined by the Sherpa guideline (www.sherpa.ac.uk/romeo/).

6. Permission granted for books and journals is granted for the lifetime of the first edition and does not apply to second and subsequent editions (except where the first edition permission was granted free of charge or for signatories to the STM Permissions Guidelines http://www.stm-assoc.org/copyright-legal-affairs/permissions/permissions-guidelines/), and does not apply for editions in other languages unless additional translation rights have been granted separately in the licence.

7. Rights for additional components such as custom editions and derivatives require additional permission and may be subject to an additional fee. Please apply to Journalpermissions@springernature.com/bookpermissions@springernature.com for these rights.

8. The Licensor's permission must be acknowledged next to the licensed material in print. In electronic form, this acknowledgement must be visible at the same time as the figures/tables/illustrations or abstract, and must be hyperlinked to the journal/book's homepage. Our required acknowledgement format is in the Appendix below.

9. Use of the material for incidental promotional use, minor editing privileges (this does not include cropping, adapting, omitting material or any other changes that affect the meaning, intention or moral rights of the author) and copies for the disabled are

permitted under this licence.

10. Minor adaptations of single figures (changes of format, colour and style) do not require the Licensor's approval. However, the adaptation should be credited as shown in Appendix below.

Appendix — Acknowledgements:

For Journal Content:
Reprinted by permission from [**the Licensor**]: [**Journal Publisher** (e.g. Nature/Springer/Palgrave)] [**JOURNAL NAME**] [**REFERENCE CITATION** (Article name, Author(s) Name), [**COPYRIGHT**] (year of publication)

For **Advance Online Publication papers:**
Reprinted by permission from [**the Licensor**]: [**Journal Publisher** (e.g. Nature/Springer/Palgrave)] [**JOURNAL NAME**] [**REFERENCE CITATION** (Article name, Author(s) Name), [**COPYRIGHT**] (year of publication), advance online publication, day month year (doi: 10.1038/sj.[JOURNAL ACRONYM].)

For Adaptations/Translations:
Adapted/Translated by permission from [**the Licensor**]: [**Journal Publisher** (e.g. Nature/Springer/Palgrave)] [**JOURNAL NAME**] [**REFERENCE CITATION** (Article name, Author(s) Name), [**COPYRIGHT**] (year of publication)

Note: For any republication from the British Journal of Cancer, the following credit line style applies:

Reprinted/adapted/translated by permission from [**the Licensor**]: on behalf of Cancer Research UK: : [**Journal Publisher** (e.g. Nature/Springer/Palgrave)] [**JOURNAL NAME**] [**REFERENCE CITATION** (Article name, Author(s) Name), [**COPYRIGHT**] (year of publication)

For **Advance Online Publication** papers:
Reprinted by permission from The [**the Licensor**]: on behalf of Cancer Research UK: [**Journal Publisher** (e.g. Nature/Springer/Palgrave)] [**JOURNAL NAME**] [**REFERENCE CITATION** (Article name, Author(s) Name), [**COPYRIGHT**] (year of publication), advance online publication, day month year (doi: 10.1038/sj.[JOURNAL ACRONYM])

For Book content:
Reprinted/adapted by permission from [**the Licensor**]: [**Book Publisher** (e.g. Palgrave Macmillan, Springer etc) [**Book Title**] by [**Book author**(s)] [**COPYRIGHT**] (year of publication)

Other Conditions:

Version 1.0

Questions? customercare@copyright.com or +1-855-239-3415 (toll free in the US) or +1-978-646-2777.